

MASARYKOVA UNIVERZITA
PŘÍRODOVĚDECKÁ FAKULTA
ÚSTAV TEORETICKÉ FYZIKY A ASTROFYZIKY

Bakalářská práce

BRNO 2022

MARIANNA DAFČÍKOVÁ

Modeling the Low Earth Orbit Particle Background of GRBAAlpha using Space Weather Data

Bakalářská práce

Marianna Dafčíková

Bibliografický záznam

- Autor:** Marianna Dafčíková
Přírodovědecká fakulta, Masarykova univerzita
Ústav teoretické fyziky a astrofyziky
- Název práce:** Modelování částicového pozadí GRBAlpha na nízké oběžné dráze pomocí dat kosmického počasí
- Studijní program:** Fyzika
- Studijní obor:** Astrofyzika
- Vedoucí práce:** Mgr. Jean-Paul Bernhard Riffald Souza Breuer
- Akademický rok:** 2021/2022
- Počet stran:** x + 48
- Klíčová slova:** GRBAlpha; kosmické počasí; částicové pozadí nízké oběžné dráhy; zesílení radiačního pásu; geomagnetická bouře; událost slunečních energetických částic

Bibliographic Entry

Author: Marianna Dafčíková
Faculty of Science, Masaryk University
Department of Theoretical Physics and Astrophysics

Title of Thesis: Modeling the Low Earth Orbit Particle Background of GRBAlpha using Space Weather Data

Degree Programme: Physics

Field of Study: Astrophysics

Supervisor: Mgr. Jean-Paul Bernhard Riffald Souza Breuer

Academic Year: 2021/2022

Number of Pages: x + 48

Keywords: GRBAlpha; space weather; low Earth orbit particle environment; radiation belt enhancement; geomagnetic storm; solar energetic particle event

Abstrakt

Představujeme studii vlivů kosmického počasí v prostředí nízké oběžné dráhy Země (LEO), pozorovaného CubeSatem GRBAAlpha. Zkoumáme dvě zesílení radiačního pásu (RBE), jednu událost slunečních energetických částic (SEP) a jednu geomagnetickou bouři (GST). Hlavní pozorované příspěvky jsou vyšší tok částic ve vnějším radiačním pásu od RBE, zvýšená populace vysokoenergetických částic v oblastech polárních kapes od SEP a dlouhotrvající proniknutí částic z vnitřního radiačního pásu do nižších nadmořských výšek od GST. Zjistili jsme, že NASA/NOAA definice událostí vesmírného počasí nejsou dostatečné pro prostředí LEO a budou muset být upraveny pro budoucí analýzu prostředí LEO. Na závěr diskutujeme ztrátu VHF rádia vysoce pravděpodobně způsobenou událostí SEP 28. října 2021.

Abstract

We present a study of the space weather effects in low Earth orbit (LEO) environment as experienced by the GRBAAlpha CubeSat. Two radiation belt enhancements (RBEs), one solar energetic particle (SEP) event and one geomagnetic storm (GST) are investigated. The main observed contributions are the increase in particle flux within the outer radiation belt by RBEs, enhanced high-energy particle population in polar cusp regions by SEPs, and long-lasting precipitation of inner belt particles to lower altitudes by GSTs. We have found that NASA/NOAA definitions of space weather events are not sufficient for the LEO environment and will have to be modified for future analysis of the LEO background. Finally, we discuss a highly probable VHF radio loss caused by the SEP event on October 28, 2021.

ZADÁNÍ
BAKALÁŘSKÉ PRÁCE

Akademický rok: 2021/2022

Ústav:	Ústav teoretické fyziky a astrofyziky
Studentka:	Marianna Dafčíková
Program:	Fyzika
Specializace:	Astrofyzika

Ředitel *ústavu* PŘF MU Vám ve smyslu Studijního a zkušebního řádu MU určuje bakalářskou práci s názvem:

Název práce:	Modeling the Low Earth Orbit Particle Background of GRB Alpha using Space Weather Data
Název práce anglicky:	Modeling the Low Earth Orbit Particle Background of GRB Alpha using Space Weather Data
Jazyk závěrečné práce:	angličtina

Oficiální zadání:

GRBAlpha is a new cube sat that was launched in March 2021 with the main objective of characterizing the background and degradation of the gamma ray detectors. The secondary objective was to attempt to detect gamma ray bursts (GRB). This secondary objective can be a challenge if we do not understand the particle background experienced by the onboard instruments sufficiently well enough, as a small burst might be interpreted as noise or misinterpreted as another feature of the radiation environment during its low earth polar orbit. Using the same data used by the Heliophysics and Space Weather group at NASA, we seek to explore the effects of Space Weather on the local earth environment, specifically with focus on how these particular events effect the background of the particle detector instruments onboard the satellite. We hope to improve the background model that we are currently using, to adjust for any potential events in the future, so that we can increase the sensitivity and significance of GRB detection.

Vedoucí práce:	Jean-Paul Bernhard Riffald Souza Breuer
Konzultant:	RNDr. Jakub Řípa, Ph.D.
Datum zadání práce:	10. 11. 2021
V Brně dne:	23. 5. 2022

Zadání bylo schváleno prostřednictvím IS MU.

Marianna Dafčíková, 15. 12. 2021

Jean-Paul Bernhard Riffald Souza Breuer, 12. 1. 2022

RNDr. Luboš Poláček, 14. 1. 2022

Acknowledgement

I would like to express my sincere gratitude to Jean-Paul and Jakub for their precious time, enthusiastic guidance, never-ending encouragement, and patience every step of the way.

Also, a huge thank you belongs to my family, friends and partner for believing in me at all times.

Prohlášení

Prohlašuji, že jsem svoji bakalářskou práci vypracoval(-a) samostatně pod vedením vedoucího práce s využitím informačních zdrojů, které jsou v práci citovány.

Brno 23. května 2022

.....
Marianna Dafčíková

Contents

List of Abbreviations	ix
Introduction	1
Chapter 1. Heliophysics and space weather	2
1.1 The Sun	2
1.1.1 Solar magnetic field	2
1.1.2 Solar wind	4
1.1.3 Solar eruptions	5
1.2 Earth’s magnetosphere	7
1.2.1 Van Allen radiation belts	9
1.2.2 Particle injection into magnetosphere	10
1.3 Space weather events	11
Chapter 2. Data acquisition	13
2.1 GRBAlpha	13
2.1.1 Gamma-ray detector	13
2.1.2 SatNOGS	15
2.1.3 Supplementary VZLUSAT-2 data	15
2.2 DONKI	15
2.3 iSWA	15
Chapter 3. Methods and data analysis	16
3.1 Data introduction	16
3.1.1 LEO environment	16
3.1.2 Time series data	19
3.2 Background model	19
3.2.1 Data binning	20
3.2.2 Interpolation	23
3.3 Statistical analysis	23
3.3.1 Skewed distributions	25
Chapter 4. Results and discussion	29
4.1 Radiation belt enhancements in April 2021	29
4.1.1 Event overview	29

4.1.2 GRBAlpha observations	29
4.2 Solar energetic particle event on October 28, 2021	34
4.2.1 Event overview	34
4.2.2 GRBAlpha observations	34
4.2.3 VHF radio loss	36
4.3 Geomagnetic storm on March 13, 2022	38
4.3.1 Event overview	38
4.3.2 GRBAlpha observations	38
4.3.3 VZLUSAT-2 observations	39
4.4 Elevated count rate between the SAA and north polar ring	42
Conclusion and future insights	44
Bibliography	48

List of Abbreviations

ACE	Advanced Composition Explorer
ADC	analog-to-digital converter
bgd	background
CAMELOT	CubeSats Applied for MEasuring and LOcalising Transients
CH	coronal hole
CME	coronal mass ejection
COM	communication UHF transceiver
cps	counts per second
CsI(Tl)	thallium activated cesium-iodide
DONKI	Database Of Notifications, Knowledge, Information
DSCOVER	Deep Space Climate Observatory
E	energy
eV	electronvolt
EUV	extreme ultraviolet
GEO	geostationary orbit
GOES	Geostationary Operational Environmental Satellite
GPS	Global Positioning System
GRB	gamma-ray burst
GST	geomagnetic storm
HSS	high speed stream
IPS	interplanetary shock
iSWA	iNtegrated Space Weather Analysis
K	Kelvin
LEO	low Earth orbit
MCU	microcontroller unit
MPC	magnetopause crossing
MPPC	Multi-Pixel Photon Counter
NASA	National Aeronautics and Space Administration
NOAA	National Oceanic and Atmospheric Administration
NP	north pole

OBC	on-board computer
pfu	particle flux unit
R_E	Earth's radius
RBE	radiation belt enhancement
SAA	South Atlantic Anomaly
SatNOGS	Satellite Networked Open Ground Station
SDO	Solar Dynamics Observatory
SEP	solar energetic particle
SNR	signal-to-noise ratio
SOHO	Solar and Heliospheric Observatory
SP	south pole
std	standard deviation
t_{exp}	exposure time
UV	ultraviolet
UHF	ultra high frequency
VHF	very high frequency

Introduction

GRBAlpha is a CubeSat mission which aims to demonstrate the performance of a newly developed gamma-ray detector for future CAMELOT mission with a primary goal to accurately localize gamma-ray bursts (GRBs). This will enable their subsequent observations with different instruments, and thus provide better understanding of their origin.

In order to accurately identify all detected GRBs, proper understanding of the background is necessary. To achieve this, a real-time characterization of the conditions will be crucial in future operations. Being on a Sun-synchronous low Earth polar orbit, GRBAlpha experiences a dynamic environment of the Earth's radiation belts. As the Earth's magnetosphere is a very complex and interconnected system, different regions within it directly affect each other. Thus, the environment experienced by LEO satellites is subject to much magnetospheric variation.

The shape of the magnetosphere is predominantly determined by the the solar wind conditions in interplanetary space. Small variations are present at all times, however, when the conditions get intense, the entire magnetosphere changes drastically. The primary driver of the dynamics in the interplanetary medium is the sun and its activity. The impacts it has on the near-Earth space is what we call space weather.

As the sun is headed to the maximum of its activity, now it becomes more and more important to have a thorough understanding of its influences. In this work, we intend to investigate the effects of space weather on the LEO environment, in order to make our background model more flexible for future missions.

Chapter 1

Heliophysics and space weather

1.1 The Sun

Energy is generated in the core of the sun primarily by a proton-proton fusion process which takes four hydrogen nuclei to produce helium. During the process, electromagnetic radiation is produced in form of gamma photons (Carroll and Ostlie, 2006). To get to the solar surface, generated photons must propagate through radiation and convection zones. A high plasma density in the radiation zone results in short mean free paths for photons which are consequently absorbed and re-emitted continuously for up to hundreds of thousands of years. In the convection region, energy is transported in convective cells, which are slightly hotter areas than their surroundings, and therefore move upward to cooler parts of the Sun while generating convection currents. The tips of these currents can be seen in the photosphere, the Sun's lowest atmospheric layer, as a granulation pattern (Beedle et al., 2022).

The solar atmosphere consists of three distinct layers, respectively the photosphere, chromosphere and corona. This division is closely related to temperature variations. In the photosphere, also referred to as the solar surface, as most of the radiation is emitted from this region, the temperature decreases with altitude reaching the lowest values of about 4400 K at its peak, approximately 600 km above the convection zone. At this boundary, the temperature propagation reverses and rises throughout the chromosphere up to about 10^4 K. In the chromosphere–corona transition region, the temperature rapidly reaches 10^5 K in only about 100 km. The top layer, the corona, is an extremely hot environment with temperatures in orders of 10^6 K spreading to the entire solar system (Carroll and Ostlie, 2006).

1.1.1 Solar magnetic field

The solar magnetic field is a dynamic environment whose origin is not yet fully understood. The main hypothesis is that it is generated by a dynamo process in which kinetic energy is converted to electromagnetic energy. In the case of the Sun, the kinetic energy comes from flows in the convection zone and solar differential rotation (Schrijver et al., 2019). Differential rotation means that the solar equator rotates faster than higher latitude regions. The periods vary from approximately 25 days at the equator to 30 days at poles.

The differential rotation stretches the magnetic field lines which consequently wrap around the Sun. After several rotations, field lines begin to twist and develop into magnetic flux tubes, regions of highly concentrated magnetic fields. Large flux tubes can penetrate into the surface and form a magnetic loop. At these locations where the tubes enter the photosphere, groups of sunspots emerge. The stronger magnetic field prevents heat flow and therefore the temperature of these areas decreases, which is why they appear darker, in contrast to their surroundings, in optical images (Beedle et al., 2022).

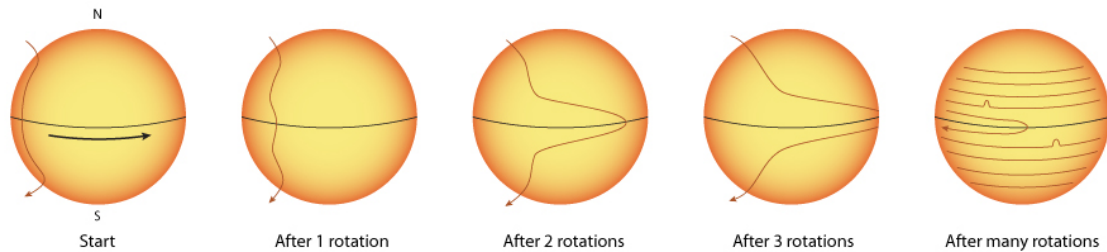


Figure 1.1: Graphical representation of magnetic field line distortion under the influence of solar differential rotation. Source: ESA/CESAR (2022).

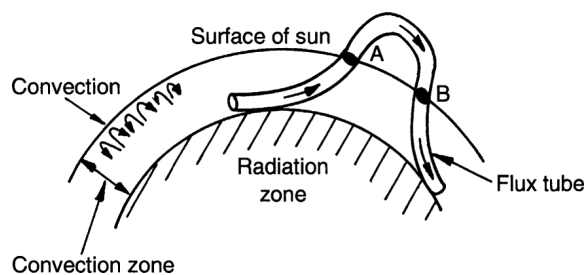


Figure 1.2: An illustration of sunspot pair emergence. Source: Davidson (2016).

Once in about 11 years, a period referred to as the solar cycle, the solar magnetic poles reverse. This happens at solar maximum when the solar magnetic field is much more complex and its activity more frequent. On the contrary, during solar minimum the field is relatively simple, similar to that of a dipole (Carroll and Ostlie, 2006). The differences between quiet and disturbed solar magnetic fields is demonstrated in Fig. 1.3.

Closed magnetic field lines which are tied to the Sun by both ends form sunspot groups, also named active regions, as the majority of extreme solar activity originates here. On the other hand, open field lines are connected to the Sun only via one end, leaving the other to extend far into the interplanetary space. These regions, called coronal holes (CHs), appear darker in EUV and soft X-ray images which is due to lower temperatures compared to the ambient corona. Their lower density allows particles to get through the chromosphere–corona transition region faster and escape into the interplanetary space (Beedle et al., 2022).

Although particles leave the Sun radially, the rotation of the Sun creates a spiral geometry in the interplanetary magnetic field (IMF) referred to as the Parker spiral. IMF lines cross the Earth's orbit at an angle of approximately 45 degrees from the Sun–Earth line. Because the Sun's global magnetic field is predominantly dipolar, the IMF also has

a dipolar structure. Locations where the polarity changes are defined by the heliospheric current sheet (Aran et al., 2018).

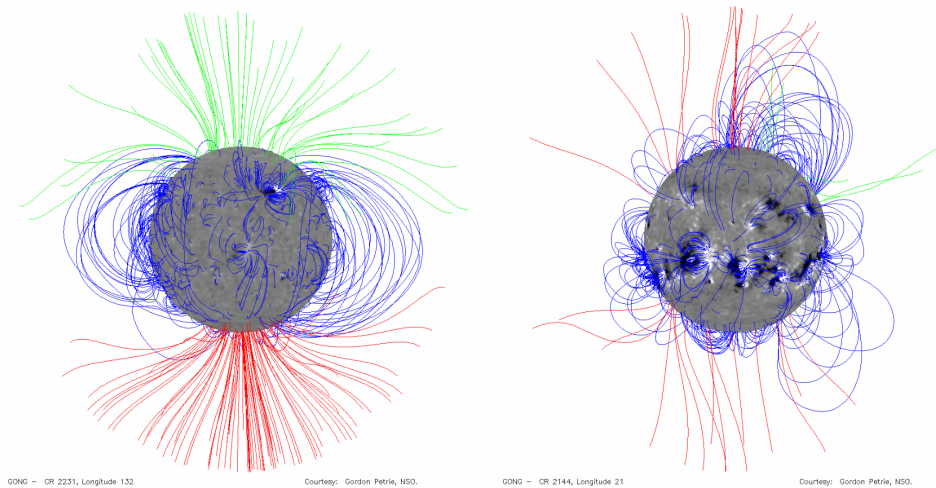


Figure 1.3: Example of quiet (left) and disturbed (right) global solar magnetic field from Potential-field Source-surface (PFSS) model by Petrie et al.¹ Closed magnetic field lines are shown in blue, open positive and negative field lines in green and red, respectively.

1.1.2 Solar wind

The solar wind, a constant stream of plasma from the solar corona, is classified into two different categories. The fast solar wind, with average speeds of 800 km s^{-1} , originates in coronal holes; while the slow solar wind seems to be related to various regions of closed magnetic field lines and typically flows at around 450 km s^{-1} .

Fast coronal hole solar winds are referred to as high speed streams (HSSs). As they propagate outward from the Sun, they interact with the ambient slow solar wind and create so-called stream interaction regions of stronger pressure which compresses the plasma at their front boundary. If the speed difference of slow and fast wind exceeds local magnetosonic speed, a shock will be formed in the front (Schrijver et al., 2019).

Generally, there are two large CHs around the magnetic poles where the dipole-like field lines diverge. They can persist for several years around solar minimum. During high solar activity, CHs often tear apart and move to lower latitudes, but as the magnetic field is very dynamic, they then develop and dissolve more quickly. Therefore, high speed streams are major contributors to space weather at solar minimum while more eruptive events dominate during the maximum phase (Temmer, 2021).

¹Downloaded from [iSWA System](#).

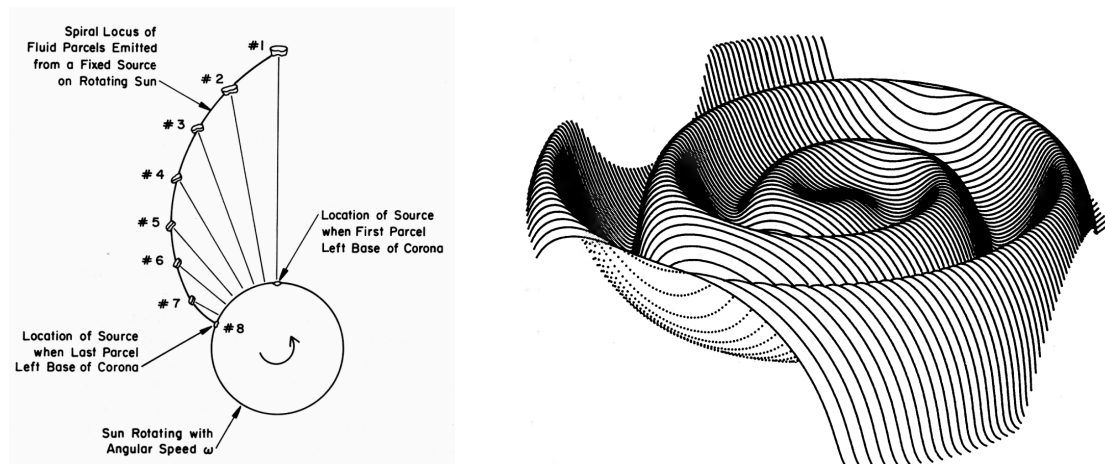


Figure 1.4: *Left:* An illustration of Parker spiral formation. Source: [Kivelson and Russell \(1995\)](#). *Right:* Heliospheric current sheet modelled by [Jokipii and Thomas \(1981\)](#).

1.1.3 Solar eruptions

A solar eruption is an intense energy release from the corona initiated by various plasma instabilities. The most important process responsible for the release is thought to be magnetic reconnection. Its fundamental principle is the conversion of magnetic energy to other forms. Under normal conditions, the field lines cannot mix together so when oppositely directed field lines approach, magnetic energy begins to build up at their boundary. The changing magnetic field induces electrical current and consequently a thin current sheet between the two domains arises. Once the amount of accumulated energy reaches certain threshold, the field lines merge and particles are accelerated in two opposite directions. Part of them falls back towards the sun to heat and brighten the chromosphere, the rest is accelerated into the interplanetary space as a cloud of magnetized plasma. The result of a magnetic reconnection in solar corona is either a solar flare or a coronal mass ejection (CME) ([Hughes, 2014](#); [Beedle et al., 2022](#)). The difference in the process leading to a flare or to a CME remains unknown. Flares and CMEs often accompany each other, however, both have also been observed independently of one another.

Solar flares

Flares are usually short-lasting, from several seconds to a few hours. Because they are bursts of electromagnetic energy, spanning the entire spectrum, they travel at the speed of light, reaching the Earth in approximately eight minutes. Flare classification ([Tab. 1.1](#)) is based on the peak X-ray flux measured by the GOES satellites in the 0.1 – 0.8 nm band, with the classification ranging from least to most energetic events, respectively A, B, C, M, and X class flares. Moreover, each flare is assigned a number between 1 and 9 depending on the exact peak flux value ([Beedle et al., 2022](#)); however, sometimes the most powerful events far exceed the average fluxes for this classification. In such cases, flares are placed into the X class with the number corresponding to the actual peak flux in order of 10^{-4} W m^{-2} . The most intense solar flare in recorded history was an X28 flare which erupted during the 2003 Halloween storms ([Gopalswamy, 2017](#)).

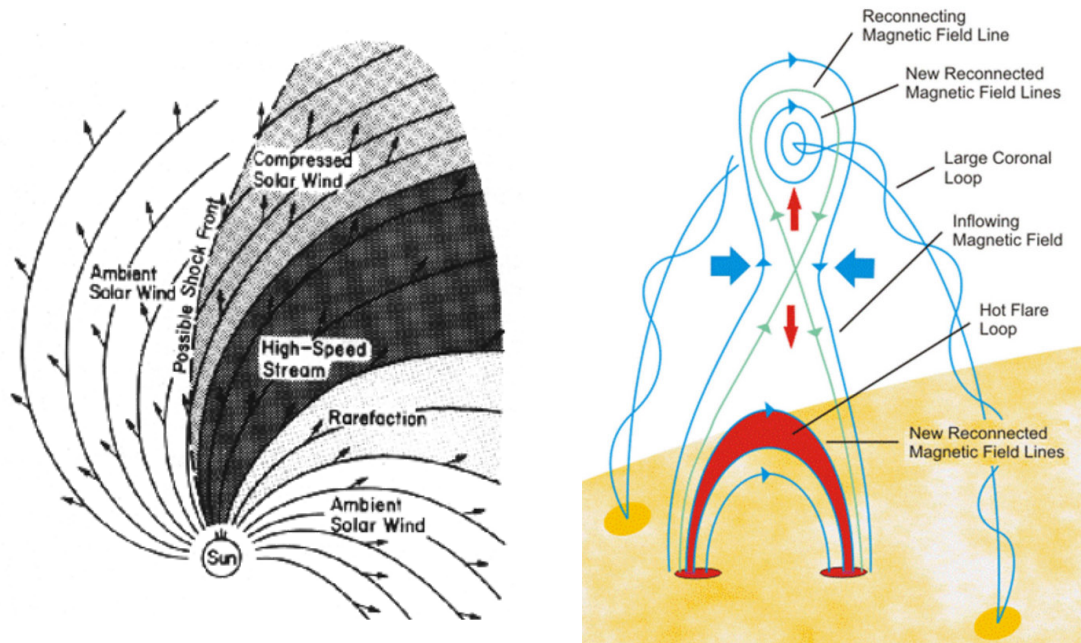


Figure 1.5: An illustration of stream interaction region by [Hundhausen \(1972\)](#) (left) and the process of magnetic reconnection in solar atmosphere (right, [NASA \(2015\)](#)).

Table 1.1: Classification of solar flares.

solar flare class	GOES X-ray flux [W m^{-2}]
A	$10^{-8} - 10^{-7}$
B	$10^{-7} - 10^{-6}$
C	$10^{-6} - 10^{-5}$
M	$10^{-5} - 10^{-4}$
X	$10^{-4} - 10^{-3}$

Coronal mass ejections

CME classification (Tab. 1.2) is derived from their speed, which can be estimated from at least two coronagraphs with different viewpoints of the sun. Their arrival times at Earth's orbit vary from more than four days for the slowest ones to only several hours for the fastest ([Evans et al., 2013](#)).

Whether a CME will or will not hit the Earth depends particularly on the active region location and the CME angular width. In coronagraph images from spacecrafts in near-Earth space, such as SOHO, Earth-directed CMEs appear as halo CMEs. However, multiple viewpoints are needed to determine the direction of their propagation because a halo CME can also move in the exact opposite direction ([Kim et al., 2008](#)).

Solar energetic particles

Solar energetic particle (SEP) events are enhancements in electron and ion, especially proton, fluxes. We distinguish between two SEP event types based on particle acceleration mechanism. Impulsive SEPs are accelerated during magnetic reconnection processes

Table 1.2: Classification of coronal mass ejections.

CME type	CME speed [km s ⁻¹]	time arrival at Earth's orbit
S	< 500	> 3.5 days
C	500 – 999	3.5 – 1.7 days
O	1000 – 1999	42 – 21 hours
R	2000 – 2999	21 – 14 hours
ER	> 3000	< 14 hours

resulting in a flare. They are characterized by a rapid onset but low intensity and short duration. On the contrary, gradual SEPs are more powerful and last up to several days. These are accelerated by fast CME-driven shock waves. In reality, majority of SEP events are associated with both, initiated by a flare while subsequent CME prolongs the acceleration process and therefore also SEP event duration.

Regardless of the exact mechanism, SEPs are accelerated to high relativistic speeds. The most powerful ones will reach the Earth's orbit in only ten minutes and the others usually within an hour. To identify SEP events, NOAA and NASA use proton flux data measured by GOES satellites in two energy bands. Threshold levels are 10 pfu for energies $E > 10$ MeV and 1 pfu for $E > 100$ MeV.²

SEP events that impact the Earth are of high concern because they can damage space-based technology and expose astronauts to higher radiation doses. One important factor to look at here is the magnetic connectivity of the source active region to the Earth. Due to the shape of Parker spiral, SEPs originating in western side of the solar disk are most geoeffective. Intense and well connected SEPs can also cause a ground level enhancement, increased radiation detected by neutron monitors on the ground (Temmer, 2021).

1.2 Earth's magnetosphere

Earth's magnetic field is generated by convection currents in its outer liquid core. Close to the Earth, its shape is very similar to that of a dipole with axis tilted about 11 degrees from the rotational axis and slightly displaced from the planet's center. Similarly to the sun, the Earth's magnetic field also experiences pole reversals, however, they are much less frequent. Currently, the Earth's north magnetic pole is located near the geographical south pole and vice versa. Therefore, field lines are oriented in a northward direction. At greater distances, the magnetosphere's structure is predominantly determined by the interaction with the solar wind (Hughes, 2014).

On the dayside, the field is compressed to a distance of about 15 R_E (de Pater and Lissauer, 2015). There, the supersonic solar wind first interacts with geomagnetic field resulting in a shock wave, called the bow shock, where the solar wind particles are slowed down and their kinetic energy is converted to thermal energy. This creates a hot and dense environment, sort of a transition region between the pure magnetospheric plasma and the interplanetary medium, called the magnetosheath. The sunward boundary of the plasma region controlled by the Earth's magnetic field is defined by the magnetopause where the

²pfu = particles cm⁻² s⁻¹ sr⁻¹

two media are at pressure equilibrium. Its location is approximately at $10 R_E$ during mild conditions, however, it can be compressed to much lower altitudes and possibly cross the geostationary orbit (GEO) at $6.6 R_E$, where it can pose a hazard for satellites and spacecraft (Beedle et al., 2022). In the event that the magnetopause is close to GEO orbits, a warning for magnetopause crossing is issued.

On the nightside, geomagnetic field is stretched into a tail-like structure, the magnetotail, which can extend to distance of hundreds of Earth's radii at times of severe solar activity. The magnetotail consists of two regions of stronger magnetic field and low plasma density, referred to as northern and southern lobes, separated by magnetically weaker but denser plasma sheet. This sheet plays a key role in particle injection into the inner magnetosphere. The lobes are at one end tied to polar cusps, areas of open field lines around magnetic poles where the field strength is lower and external particles can easily penetrate to lower atmospheric altitudes (Pulkkinen, 2007).

The inner magnetosphere is considered to be a region where deviations from dipolar magnetic field approximation are not very large. The innermost region is the plasmasphere which contains low energy plasma of mostly ionospheric origin. The ionosphere is the Earth's upper atmosphere ionized mostly by solar EUV radiation and by collisions with particles energetic enough to precipitate into the magnetosphere. It extends from about 80 km to nearly 1000 km above the surface and partially overlaps with low Earth orbits (LEOs, de Pater and Lissauer (2015)).

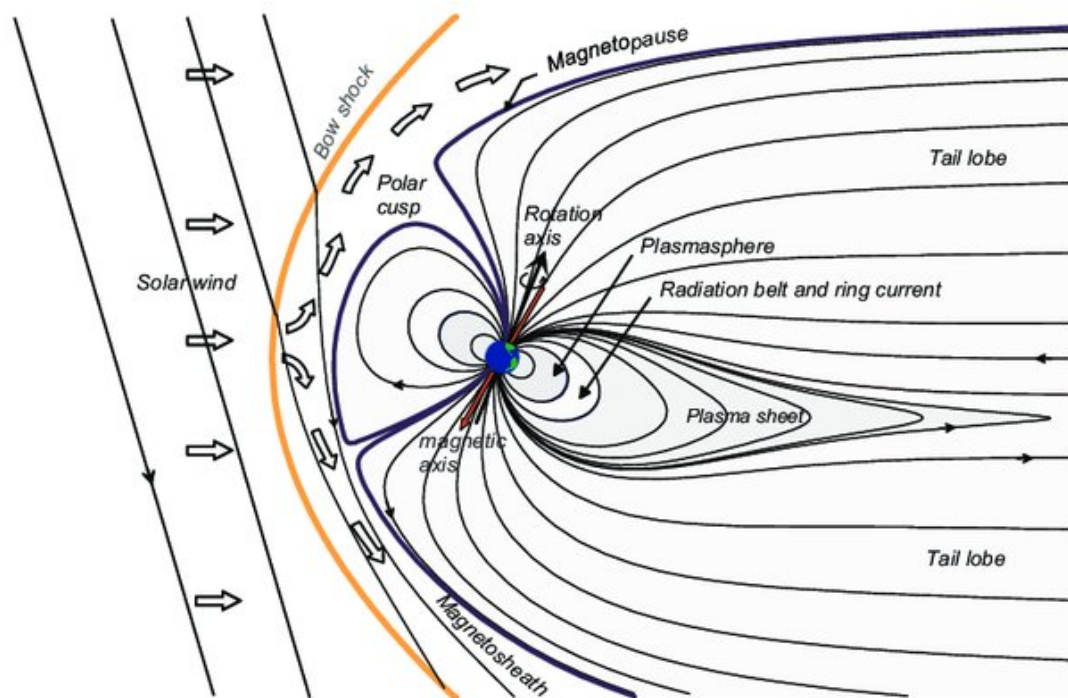


Figure 1.6: Schematic illustration of the Earth's magnetosphere. Source: Tenerani (2012).

1.2.1 Van Allen radiation belts

Two highly populated regions within the inner magnetosphere are the torus-shaped Van Allen radiation belts. The inner belt contains mostly energetic protons, though electrons are also found here. Its environment is relatively stable, located up to $2 R_E$ above the equator with maximum density at approximately 3000 km (Hughes, 2014).

Because the geomagnetic field is slightly dislocated from the Earth's center, there is a region where the inner radiation belt approaches closest to the surface, known as the South Atlantic Anomaly (SAA). Here, the geomagnetic field is at its minimum for a given altitude. Currently, its deepest point is located above Paraguay. At LEO, the most energetic particles are concentrated in the SAA region which is why many satellites turn off their instruments when passing through.

The outer belt, extending from about $3 R_E$ to $10 R_E$, is filled almost exclusively with relativistic electrons. This second belt is extremely dynamic especially because of the constantly changing solar wind conditions (Koskinen and Kilpua, 2022). Although it is mainly concentrated at high altitudes, in polar regions it reaches down to only few hundred kilometers above the surface, and is therefore detectable at polar LEOs.

During times of undisturbed interplanetary conditions, particles within the radiation belts are trapped in the Earth's magnetic field. As they move along the closed field lines, they are reflected at so-called mirror points in polar regions. This results in a bouncing movement between the poles. Typical proton energies range from few keV to 100 MeV. Electrons have a bit lower energies, up to 10 MeV, but generally the more energetic ones are part of the outer belt.

At active periods, particles can be accelerated to even higher energies and may consequently penetrate to lower altitudes. During geomagnetic storms, times of highly disturbed magnetosphere, enhanced electron and proton fluxes were observed as low as 200 km above the Earth's surface (Baker et al., 2018). Increased dynamics of the radiation belts, especially the outer one, is referred to as a radiation belt enhancement (RBE) event. A threshold for an RBE event identification is set to 10^3 pfu for electrons with energy $E > 2$ MeV detected by GOES. RBEs are long duration events which last from several days to weeks.

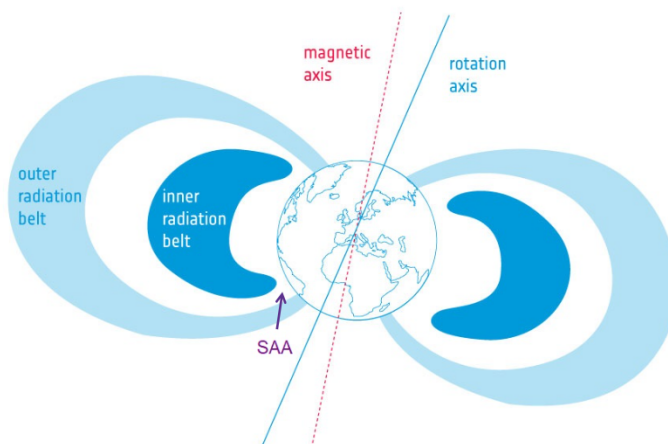


Figure 1.7: An illustration of the Van Allen radiation belts. Adapted from ESA (2016).

1.2.2 Particle injection into magnetosphere

Energetic particles most commonly enter the magnetosphere via a magnetic reconnection process at the magnetosheath–magnetopause interface. Because the geomagnetic field is directed towards the north, for a magnetic reconnection to occur, southward IMF is necessary. However, northward IMF can trigger a reconnection in polar regions where the open geomagnetic field lines are directed rather southward.

The reconnection at the dayside magnetopause opens up some of its field lines which means that polar cusps become larger as their boundary, the auroral oval, expands to lower latitudes. The reconnection process disrupts the pressure balance and as a result, the new magnetopause is compressed and plasma needs to be redistributed within the magnetosphere. Because charged particles move along the field lines, they flow into the cusps from the reconnection point, and from there to the magnetotail where pressure increases as energy is accumulated in the lobes. Once enough energy is stored, it will be released in another magnetic reconnection event. This magnetotail reconnection accelerates plasma in two opposite directions, towards and away from the Earth. The latter particles will eventually rejoin the solar wind in the interplanetary space, and are known to form some trailing plasma bubbles behind the Earth. (Pulkkinen, 2007).

Particles accelerated earthward will flow into the polar cusps with direct access to the ionosphere where they collide with atoms, and can excite or ionize them. During deexcitation and recombination, when an electron returns to its ground state while emitting a photon, the aurora is produced. The emitted photon has a wavelength corresponding to the energy of the transition between the two energy levels. This means that each chemical element and each transition between different energy levels results in uniquely colored contribution to the aurora (de Pater and Lissauer, 2015).

As the magnetosphere interacts with the solar wind and IMF, it constantly adjusts to the ram pressure and IMF conditions to maintain hydrostatic equilibrium. The continuous plasma motion induces convection within the magnetosphere. As a result, various currents flow in the magnetopause, the magnetotail, and the inner magnetosphere. All of these currents are interconnected by field-aligned currents which are particularly important in the magnetosphere–ionosphere coupling when energy, mass and momentum is transferred between the two regions (Beedle et al., 2022).

Geomagnetic storms

Depending on the duration of the dayside reconnection process and the energy accumulation in the tail lobes, magnetospheric disturbances are referred to as geomagnetic storms, if the process lasts several hours, or substorms, if the southward IMF is only present for up to an hour (Pulkkinen, 2007).

Numerous indices have been developed to determine the strength of a geomagnetic storm. For space weather predictions and analysis, the Kp index is most commonly used. It is a measure of fluctuations in the horizontal component of the Earth's magnetic field ranging from 0 to 9. As the geomagnetic conditions vary with location, the Kp index is an average of K-indices, individual values for 13 stations between 44 and 60 degrees of geomagnetic latitude. A geomagnetic storm is considered to take place if the Kp index is 5 or higher (NOAA/SWPC, 2011).

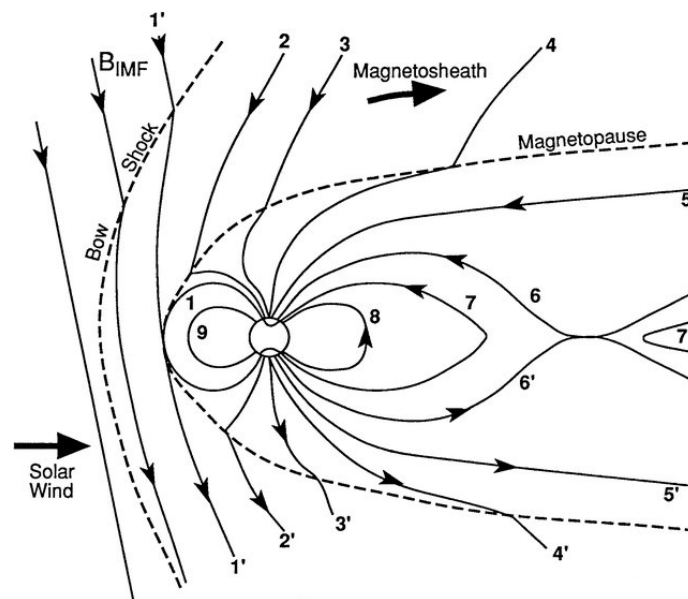


Figure 1.8: Schematic illustration of the magnetosphere interacting with the solar wind. The dayside magnetic reconnection (1) opens field lines from the magnetopause (2) which cross the polar cusps (3, 4) and enter the magnetotail (5). There, energy is being accumulated until it is released in the magnetotail reconnection (6). Part of the accelerated particles escapes to the interplanetary space (7'), the rest is captured by the Earth's magnetosphere (7–9). Source: [Kivelson and Russell \(1995\)](#).

1.3 Space weather events

NASA recognizes eight phenomena as space weather events, among them are solar flares, coronal mass ejections, solar energetic particle events, high speed streams, interplanetary shocks, magnetopause crossings, radiation belt enhancements, and geomagnetic storms. However, they rarely happen individually.

All of these events have their origins in the sun. Magnetospheric disturbances are initiated by a solar flare, CME, or a high speed stream. Solar flares increase short-wave radiation, and as well as CMEs, they can accelerate solar particles to relativistic speeds causing SEP events.

Powerful CMEs and high speed streams may cause an interplanetary shocks which can then either accelerate solar wind plasma or directly interact with the Earth's magnetosphere. Intense interplanetary conditions distort the Earth's magnetosphere by compressing the magnetopause too close to GEO orbits (MPC), increasing radiation belt dynamics (RBE), or inducing severe geomagnetic disturbances (GST). The effects of HSSs are usually less intense but longer lasting compared to the CME-driven ones.

At low earth orbit, the SEPs, RBEs and GSTs are of highest concern as they directly cause particles to penetrate to lower altitudes and interact with satellites. The highest energetic particles are able to penetrate deep into the satellite where they deposit their energy and may change the state of the device. In less severe scenarios, this can cause a bit flip in its memory, however, if the charged particle hits a more sensitive part of the spacecraft, such as the part of its memory with the software, these events can cause

permanent damage or loss of the satellite (Katz et al., 2021).

The lower energetic electrons cannot penetrate inside the spacecraft, however, they interact with the material from the spacecraft and generate a non-zero current between the satellite's surface and the ambient plasma. This can cause surface charging, which not only increases the electrical noise, but also can interrupt ongoing operations. Moreover, as the energetic particles collide with the atmosphere, the upper atmosphere can heat up and expand, causing satellites at LEO to experience a denser environment and increased drag at lower altitudes (Pulkkinen, 2007).

The enhanced current environment in the ionosphere also strongly affects signals travelling through, refracting them and slowing them down, which can lead to communication problems with satellites and GPS errors in the order of tens of meters (Ganushkina et al., 2017).

The space weather impacts, however, are not bound to space. The strong ionospheric currents may induce currents on the ground, known as geomagnetically induced currents (GICs), which may cause serious damage to systems grounded by two ends, such as power grids, oil and gas pipelines, telecommunication cables or railway systems, usually rooted in saturation of transformers (Pulkkinen, 2007). These impacts are not as rare as one might think. Numerous records of severe impacts in modern history exist, including the geomagnetic storm in 1969 when the entire power grid in Quebec collapsed in less than 90 seconds from the induction of GICs, and was not recovered for over nine hours, or the 2003 Halloween storms which caused a blackout in Sweden and damaged several transformers in Europe and Africa (Beggan et al., 2018).

To mitigate the damage caused by solar activity, it is important to constantly observe both solar and interplanetary conditions, and make predictions for near future. The satellite network dedicated to space weather forecasting and research has grown largely in past years. Here, we shortly describe those which we used in our analysis.

The Geostationary Operational Environmental Satellite (GOES) program began in 1975 with a primary mission to provide continuous atmospheric observations for weather forecasting and meteorological research. Since then, 18 spacecraft have been successfully launched into space, four of which are still in operation today. Satellites are located at geostationary orbit, meaning that their position is fixed with respect to the Earth. Apart from the main objective, satellites also carry X-ray, EUV and energetic particle sensors to observe local radiation environment (NASA/GSFC, NOAA, 2005). Currently, measurements by GOES-15 are used for space weather analysis, specifically the five-minute proton and electron data and one-minute X-ray flux data.

The Deep Space Climate Observatory (DSCOVR) and the Advanced Composition Explorer (ACE) are both located in Lagrange point L1 and their real-time solar wind and IMF observations are used as primary inputs for many forecasting models. From L1, they provide us with warnings up to an hour prior to arrival at Earth (NASA, 2002; NASA, NOAA, USAF, 2016).

Chapter 2

Data acquisition

2.1 GRBAAlpha

GRBAAlpha, launched on 22 March 2021, is a 1U CubeSat, meaning it is a cube with a $10 \times 10 \times 10 \text{ cm}^3$ volume. It operates at a Sun-synchronous orbit where it maintains the same orbit orientation with respect to the sun. The orbit's inclination is 97.5 degrees and altitude ranges from approximately 530 to 580 km. One full orbit around the Earth takes around 95 minutes.

The satellite is equipped with a gamma-ray detector developed for future CAMELOT mission which aims to provide all-high-energy-sky coverage and precisely localize gamma-ray bursts to enable their follow-up observations with instruments sensitive at other wavelengths. The primary goal of GRBAAlpha is to validate the performance and characterize the degradation of the newly developed detector.

2.1.1 Gamma-ray detector

The detector consists of an inorganic scintillator, a CsI(Tl) crystal, coupled with eight multi-pixel photon counters (MPPCs) separated into two channels (Pál et al., 2020). When a high-energy charged particle interacts with the scintillator, cesium and iodine atoms absorb its energy and as a consequence, their electrons jump from the valence band, where they leave a positively charged hole, to the conduction band, where they can move freely within the crystal lattice. The holes then ionize thallium atoms which subsequently attract the free electrons in the lattice. If the captured electron creates an excited configuration with a thallium atom, it immediately drops to the ground state while emitting a photon. This deexcitation could, in principle, take place also in a pure crystal, however, the emitted photons would be too energetic. Therefore, an activator, thallium in this case, is added to the crystal which creates its own energy states within the lattice and enables the emission of visible photons.

These photons are then detected by MPPCs, also known as a silicon photomultipliers, arrays of thousands of avalanche photodiodes connected in parallel. As the photon collides with the silicon atoms, electron-hole pairs are formed and accelerated by the strong electric field inside the photodiodes, thanks to which they produce secondary electron-hole pairs. This continues in a sort of a chain reaction what eventually amplifies the output current.

Ideally, each photodiode is hit by a maximum of one photon. In that case, the number of photodiodes contributing to the output signal, thus also its amplitude, is proportional to the number of scintillation photons (Knoll, 2000).

The output current then runs through the pre-amplifier and shaping amplifier where it is converted to voltage signal and reduced of electrical noise in order to precisely determine the pulse height which corresponds to the signal generated in the MPPC and therefore also to the energy of the incident photons. Finally, it enters the analog-to-digital converter (ADC) where it is processed to a digital form.

The approximate energies for energy bands used in the analysis throughout this work are in Tab. 2.1. The conversion between the spectral channel and energy was obtained in a pre-launch calibration with different radioactive isotopes and is as follows

$$E [\text{keV}] = 4.08 \times \text{ADC channel number} - 154 \quad (2.1)$$

Table 2.1: The conversion between energy and ADC channel for energy bands used in the analysis.

ADC channel	E [keV]
64 – 128	~ 110 to ~ 370
128 – 192	~ 370 to ~ 630
192 – 256	~ 630 to ~ 890

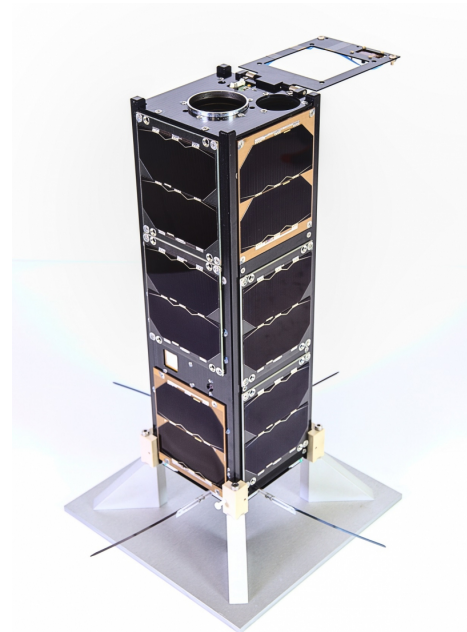


Figure 2.1: Left: GRBAlpha CubeSat.¹ Right: VZLUSAT-2 CubeSat.²

¹Downloaded from <https://grbalpha.konkoly.hu/>.

²Downloaded from <https://www.vzlusat2.cz/>.

2.1.2 SatNOGS

The Satellite Networked Open Ground Station (SatNOGS) is an open-source network of ground stations which collects telemetry signals and data automatically transmitted from many satellites, especially LEO CubeSats. This provides us with housekeeping data, such as the battery voltage or temperatures of different components, even at times when the satellite is not passing over the ground station used for regular communication. GRBAAlpha data retrieved by this network are available at [SatNOGS Dashboard](#).

In case of GRBAAlpha, the housekeeping data can be also accessed during direct communication with the satellite which is always recorded. The system current values, displayed in Fig. 4.5, were obtained from these logs, while the rest of the housekeeping data shown were obtained from the SatNOGS Dashboard.

2.1.3 Supplementary VZLUSAT-2 data

VZLUSAT-2, launched on 13 January 2022, is 3U CubeSat equipped with several instruments for monitoring the Earth and space. Among the secondary payload instruments are also two gamma-ray detectors identical to the ones that GRBAAlpha carries, except they are located under solar panels. It orbits at SSO with the same inclination as GRBAAlpha, and altitude varying between approximately 520 to 565 km what allows us to use these supplementary data to improve our background model.

2.2 DONKI

The Space Weather Database Of Notifications, Knowledge, Information (SW DONKI) collects measurements from various satellites, coronal and solar wind model outputs, and issues warnings in case of predicted severe SW conditions. The database provides records of space weather activity since 2010. DONKI identifies eight space weather event types: solar flares, SEPs, CMEs, interplanetary shocks, magnetopause crossings, geomagnetic storms, RBEs and high speed streams, and provides direct linkage between them. Data can be accessed in an [online application](#) or using an [API](#).

2.3 iSWA

The integrated Space Weather Analysis (iSWA) system is an online visualization tool developed for more convenient space weather analysis. It offers near-real time satellite data and forecasts based on numerous space weather models. The "iSWA Super Timeline" is an interactive cygnet with possibility to choose displayed data by quantity and resource. Numerical data available in this cygnet as well as image data can be downloaded using an [API](#). GOES flux data, DSCOVR solar wind speed and Kp index values used to study selected events in this work were obtained via this API.

Chapter 3

Methods and data analysis

3.1 Data introduction

Measurements analysed in this work were taken between April 14, 2021 and April 21, 2022. Since May 2021, GRBA α observations always begin with a 60 s long measurement with full spectral resolution (256 bins). The rest of the observation set is usually done in four spectral bands and with exposure time of 4 s. Few sets were done with 1 s, and one set with 60 s, exposures. In April 2021, various combinations of exposure time and spectral resolution were used including 4, 8, 32, 64, and 256 spectral bins and 1, 2, 4, 15, 40, 60, and 120 s exposures.

The measurements with high spectral resolution (64 and 256 bins) are done to characterize the long-term degradation of the detector and therefore contain only few data points, typically one or two, and were left out of the analysis. Those taken in 8 and 32 spectral bins were summed to match the four bins which are currently being used. The lowest energy band, ADC channel 0 to 64, is not considered in the analysis because of an instrumental noise peak around 45 ADC. All the measurements with 120 s exposures are only available for ADC < 128. Moreover, six sets of measurements with bad time synchronization are also not included in the analysis.

VZLUSAT-2 observations also begin with a full spectral resolution and continue measurements in the same four energy bands as GRBA α . However, the exposure time is usually either 1 or 15 s. Exact numbers of data points, examined in this work, for each exposure time are in Tab. 3.1. At the beginning, the data were normalized and all the analysis is done using count rate data, unless stated otherwise.

Fig. 3.1 displays the amount of data taken over one year. Most of the observations were done in April, July, and October 2021. In November, there is an apparent gap in the data caused by a loss of the VHF radio during the night from 29 to 30 October. This event is further discussed in Sec. 4.2.3. Since then, the UHF radio has been used for both, uplink and downlink, and the overall communication has been worse.

3.1.1 LEO environment

Fig. 3.2 shows the sky coverage of the data. Maps are displayed in all three energy bands and both, GRBA α and VZLUSAT-2, measurements are included.

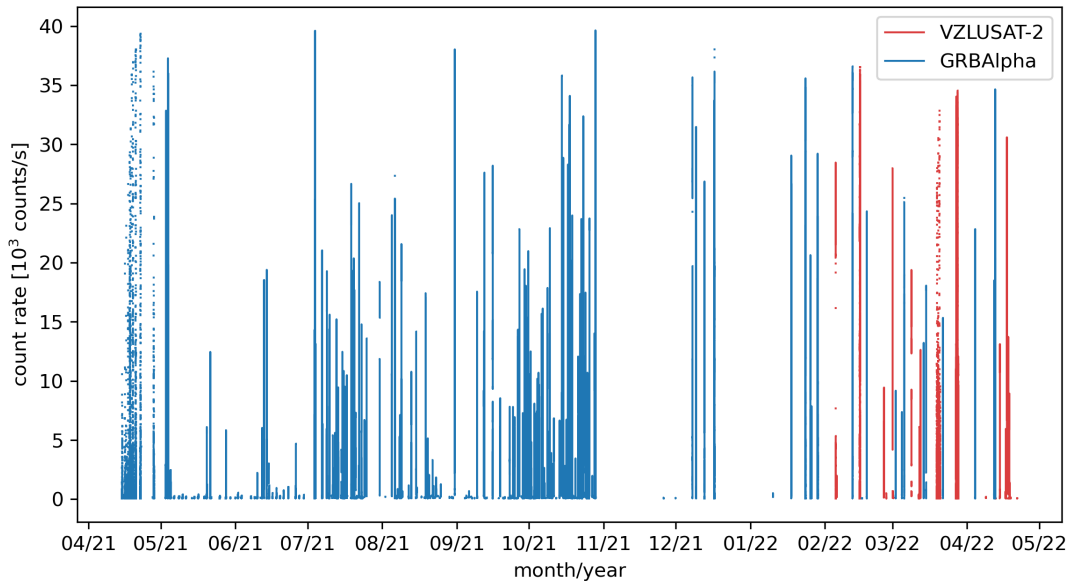


Figure 3.1: A time plot of all GRBAAlpha and VZLUSAT-2 measurements taken between April 14, 2021 and April 21, 2022. The count rate values are summed over all three energy bands, thus $\sim 110 \text{ keV} < E [\text{keV}] < \sim 890$.

There are three distinct areas with higher count rate in all three maps. Two of them are around the poles, between approximately ± 40 and ± 80 degrees of latitude depending on the exact longitude. These are regions where the outer radiation belt gets closest to the Earth. The wavy shape is caused by the offset of the magnetic axis from the rotation axis. In this thesis, we refer to these regions as the northern and southern polar rings. The third region with highly elevated count rate is the SAA. It extends from approximately 270 to 30 degrees of longitude, and from 0 to -60 degrees of latitude. However, its shape is very irregular and slightly differs in each energy band.

The map in the lowest energy band also contains weaker secondary polar rings. The one in the northern hemisphere is visible mostly in middle longitudes and is a lot weaker compared to the main ring. In the southern hemisphere, the secondary ring appears to be present in all longitudes with maximum intensity between the SAA and the southern polar ring. As all observations are displayed in the map regardless of space weather conditions, in the northern hemisphere, this could be a detection of the inner radiation belt which got closer to the Earth due to magnetospheric disturbances caused by solar activity. On the other hand, as the SAA results from the inner belt, the southern secondary ring below the SAA is probably permanent.

This southern secondary ring is also apparent in the highest energy band, however, it is not as dominant as in the lowest energies, and it does not extend to all longitudes. No similar features are observed in the middle energy band.

Overall, the lowest energetic particles appear to dominate in the polar rings while the most energetic ones in the SAA. Particles from the middle energy band seem to be redistributed more or less equally between the rings and the SAA.

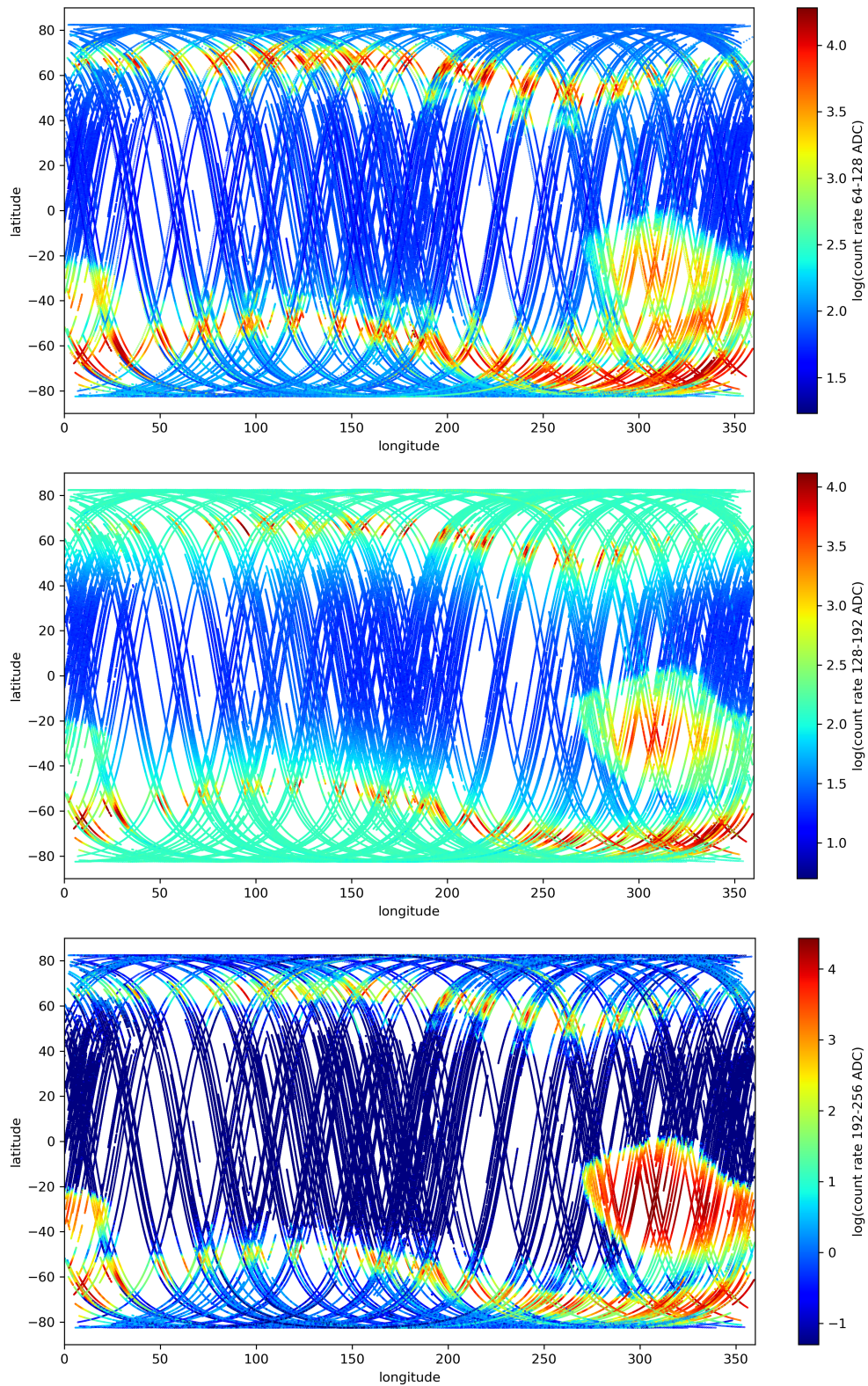


Figure 3.2: Ground tracks of GRBAAlpha and VZLUSAT-2 with count rate data shown in color. *Top:* $\sim 110 < E \text{ [keV]} < \sim 37$. *Middle:* $\sim 370 < E \text{ [keV]} < \sim 630$. *Bottom:* $\sim 630 < E \text{ [keV]} < \sim 890$.

3.1.2 Time series data

An example of time series data from GRBAAlpha is displayed in Fig. 3.3. This observation was taken during the night from 16 to 17 December 2021. During that period, there was an eruption of an M1.2 solar flare starting at 00:44¹ on December 17, however, no further space weather events were reported. The electron and proton fluxes at GOES were at background levels, and Kp index was 2 during the entire measurement.²

Shown is a full orbit around the Earth starting with a pass over the north pole, passing through the SAA and south polar ring, crossing the equator, and entering the north polar ring once more. Data are shown in all three energy bands. Clearly, the polar regions are dominated by lower energetic particles, while the SAA contains the most energetic ones. This agrees with the result from maps in Fig. 3.2, discussed in Sec. 3.1.1.

The inward cross of the southern polar ring is notably wider compared to the outward cross. This is also evident in the aforementioned maps, and it is a result of the closer approach of radiation belts in this region. Between the SAA and the southern ring, the count rate does not decrease to background values in any energy band. The lowest energetic particles exhibit one more distinct peak in this area which represents the secondary ring noticeable in the top map of Fig. 3.2.

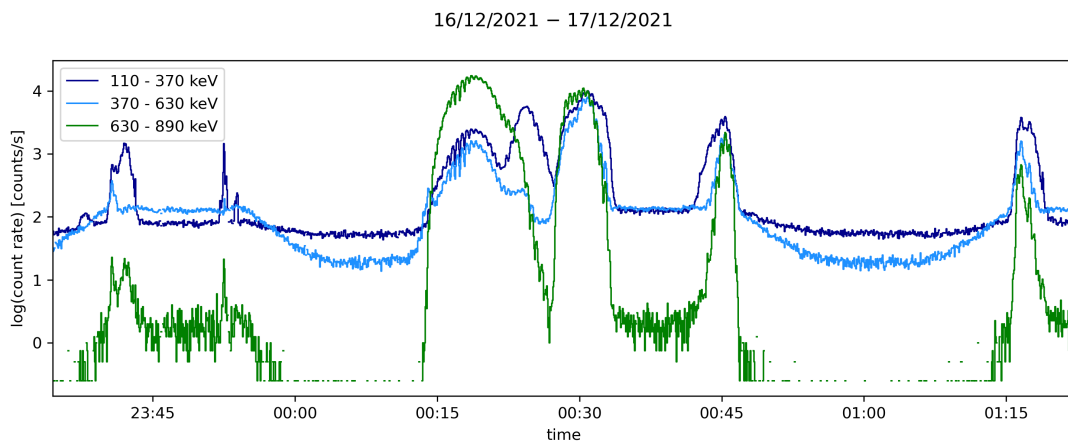


Figure 3.3: An example of time series data taken by GRBAAlpha over one orbit around the Earth during a period of low solar activity. The plot begins with a satellite pass over the north pole (first two peaks) which then continues through the SAA (widest peak starting at around 00:15) into the southern polar ring (two wider peaks in the middle) and crosses the equator to enter the north polar ring again (last peak).

3.2 Background model

In order to understand the effects of space weather events on our data, a proper definition of 'quiet' background is needed. For this purpose, we have established a simple background

¹All times referred to throughout the thesis are in Coordinated Universal Time (UTC).

²Space weather data can be reviewed at [ISWA](#).

model based on conditions for three parameters which are used for identification of RBEs, SEP events and geomagnetic storms.

RBEs are defined by the GOES electron flux for $E > 2$ MeV with threshold set to 10^3 pfu. Our threshold was chosen to be $10^{2.3}$ pfu which, as can be seen in the top part of Fig. 3.4, appears to exclude even minor increases.

An SEP event is considered to take place if the GOES proton flux exceeds 10 pfu for $E > 10$ MeV or 1 pfu for $E > 100$ MeV. From the middle part of Fig. 3.4, it is apparent that the flux in these two energy bands usually does not vary too much. On the other hand, the flux in $E > 1$ MeV highly fluctuates at all times and there is no distinct value which could be used as a threshold. Finally, our threshold level was set to 1 pfu for $E > 5$ MeV. This seems to exclude most of the peaks in this energy band, however, the fluctuations in the lowest energies are still highly present at times when flux in $E > 5$ MeV is at background level.

Geomagnetic storms are identified by the Kp index 5 or higher. In our analysis, $K_p > 3$ was chosen to define disturbed conditions within the magnetosphere. Even though in the bottom part of Fig. 3.4 it seems to be an appropriate threshold, as the Kp index is a measure of the global magnetospheric conditions, it may not always describe the conditions at the satellite's location accurately.

Maps in Fig. 3.5 show the data left after applying these conditions. Although they look very similar to those in Fig. 3.2, many artifacts have been removed, especially from inside of the polar rings.

3.2.1 Data binning

In further analysis of individual space weather events in this work, the background for a specific orbit was selected from the data which fit the three described conditions. The numbers of data points left in the background model are reviewed in Tab. 3.1.

Table 3.1: The number of GRBAlpha and VZLUSAT-2 data points for each exposure time.

t_{exp} [s]	all data		background model	
	GRBAlpha	VZLUSAT-2	GRBAlpha	VZLUSAT-2
1	17 364	23 627	13 298	4594
2	312	–	312	–
4	119 887	807	90 503	–
15	9224	21 011	940	10 053
40	131	–	19	–
60	4	–	–	–
120	626	–	504	–

For each examined data point, all measurements within a four-degree box around that point were averaged and the final number was used as the background value. Several bin sizes were tested. Those with length of two and three degrees did not cover our studied orbits sufficiently enough. The four- and five-degree bins both covered the majority of the orbits. Because the most interesting regions, the SAA and polar rings, are very dynamic and irregular, four-degree boxes were chosen in favor of higher resolution.

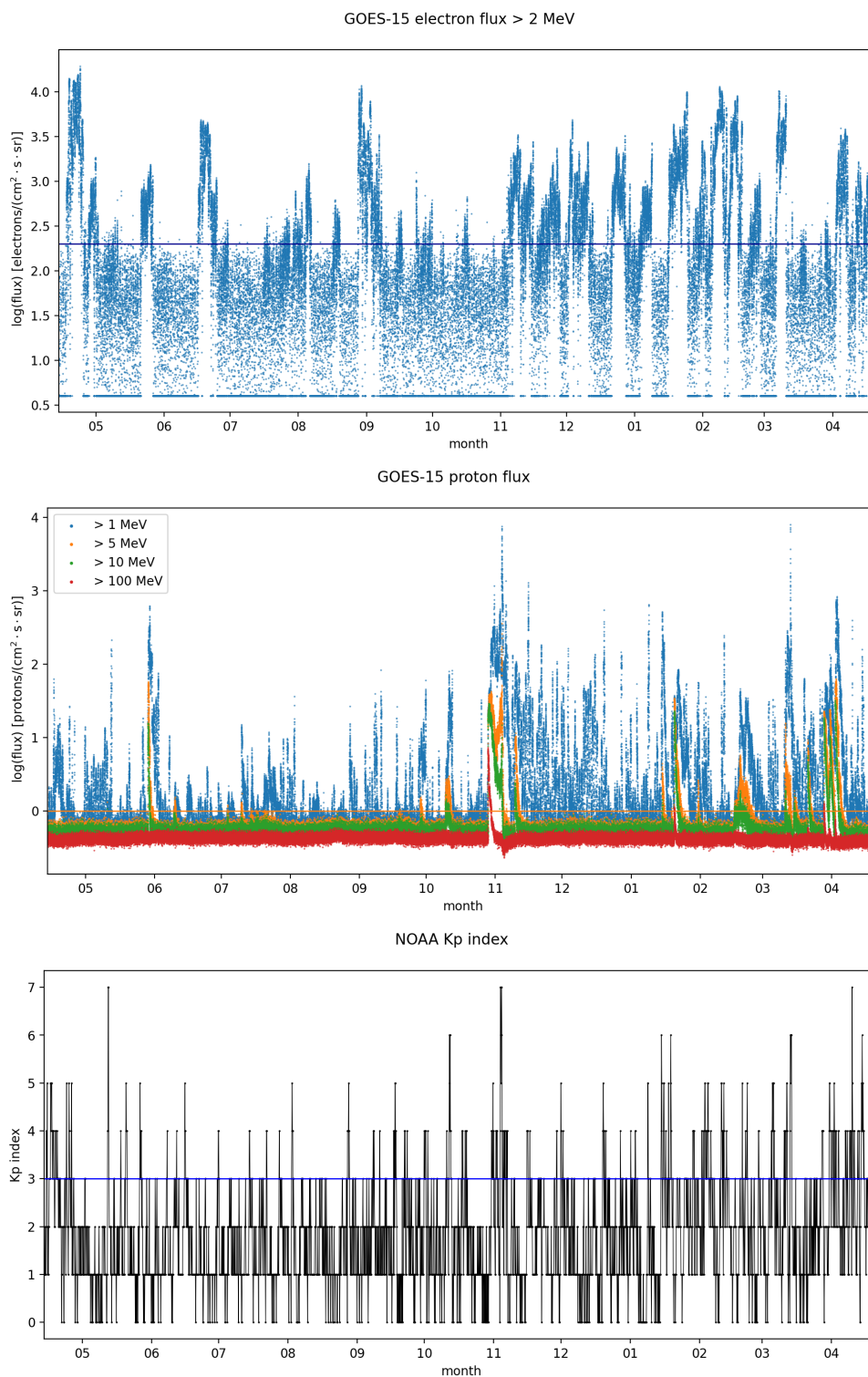


Figure 3.4: The GOES electron (top) and proton (middle) flux, and the Kp index (bottom) measured from 14 April 2021 to 22 April 2022. The horizontal lines mark the thresholds used to describe quiet background conditions at LEO.

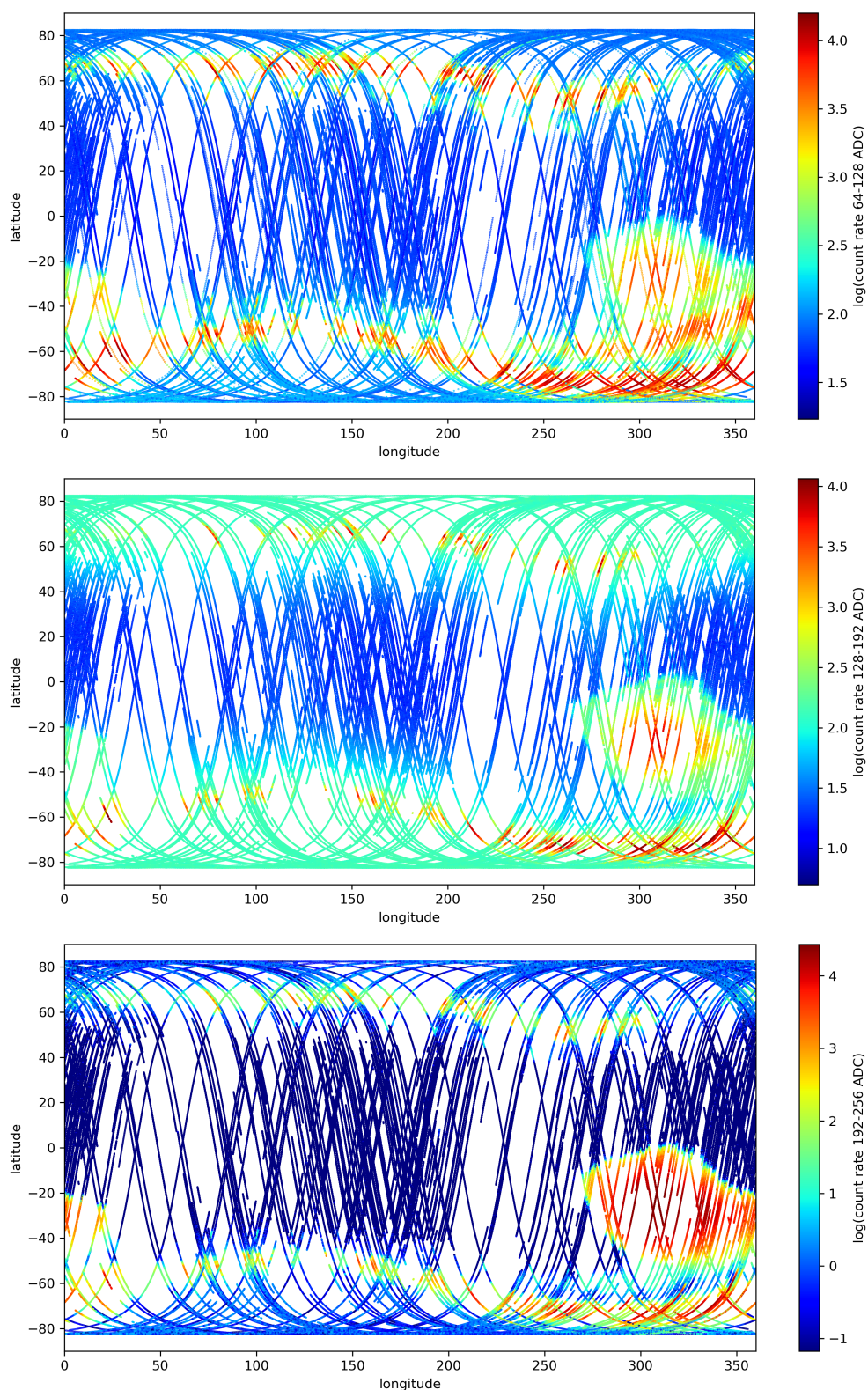


Figure 3.5: The same as Fig. 3.2 but using only data which fit our background conditions.

3.2.2 Interpolation

Another possibility of characterizing the background for a specific data point is to interpolate the data which fit our background conditions. This way, we could get a background value for any location, what is not always possible in the binning method described above, as we may not have measurements from the exact location needed. We attempted to create such model using various functions and libraries in Python but due to insufficient data coverage, the interpolated maps contained many artifacts. Therefore, we opted for the orbit-track binning method to define the background. However, one interesting thing was spotted in the interpolated maps, which is why we include this short section here.

The simplest interpolation was done using the `LinearNDInterpolator` class available in Python package `scipy.interpolate`. Fig. 3.6 shows the result for the middle energy band with a two-degree resolution. The increased count rate in the region between the SAA and the north polar ring was not observed in the interpolated maps for other energy bands. A possible explanation of this elevation is discussed in Sec. 4.4.

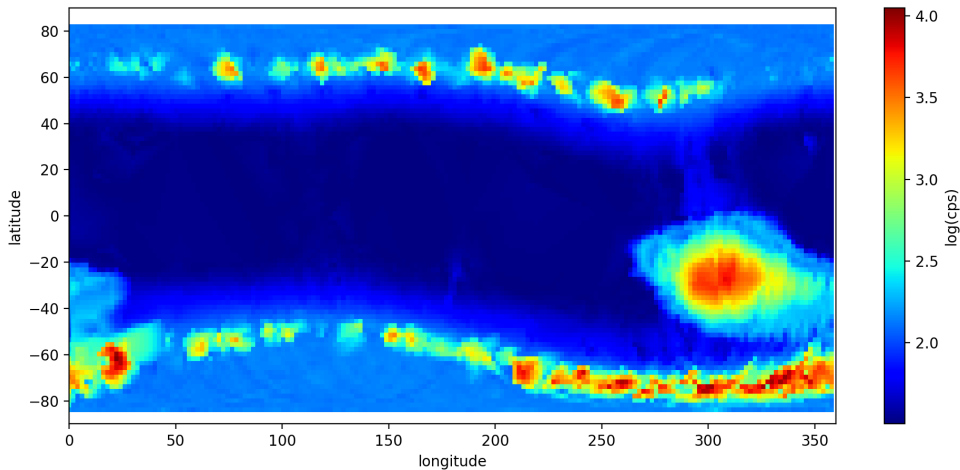


Figure 3.6: An interpolated map of the background data in the middle energy band (128 – 192 ADC).

3.3 Statistical analysis

Generally, to describe discrete data sets, such as the number of detections, the Poisson distribution is used. The standard deviation σ is then computed as

$$\sigma = \sqrt{\lambda}, \quad (3.1)$$

where λ is the average value of the set. The Poisson distribution quickly converges to normal (Gaussian), and for $\lambda \gtrsim 20$, the two distributions look very similar for the same mean and variance. The standard deviation of a Gaussian distribution is given by

$$\sigma = \sqrt{\frac{\sum_{i=1}^N (x_i - \bar{x})^2}{N - 1}}, \quad (3.2)$$

where N is the number of data points, x_i are the individual values and \bar{x} is their average.

To check whether our data follow the Poisson distribution, we calculated standard deviations according to both distributions and compared them. This was done for the background data binned into four-degree boxes, and for all three energy bands. To avoid dealing with different exposure times, only data with 4 s exposures, which make $\sim 75\%$ of all the data points from the quiet background model, were included.

The test revealed that around the equator, where the background is relatively stable at all times, our data follows the Poisson distribution. In dynamic environments, e.g. the SAA and polar regions, the difference in standard deviation computed from the two formulas, is in order of thousands. This suggests that in high background regions, a non-statistical noise is present, caused by the variability of the radiation belts.

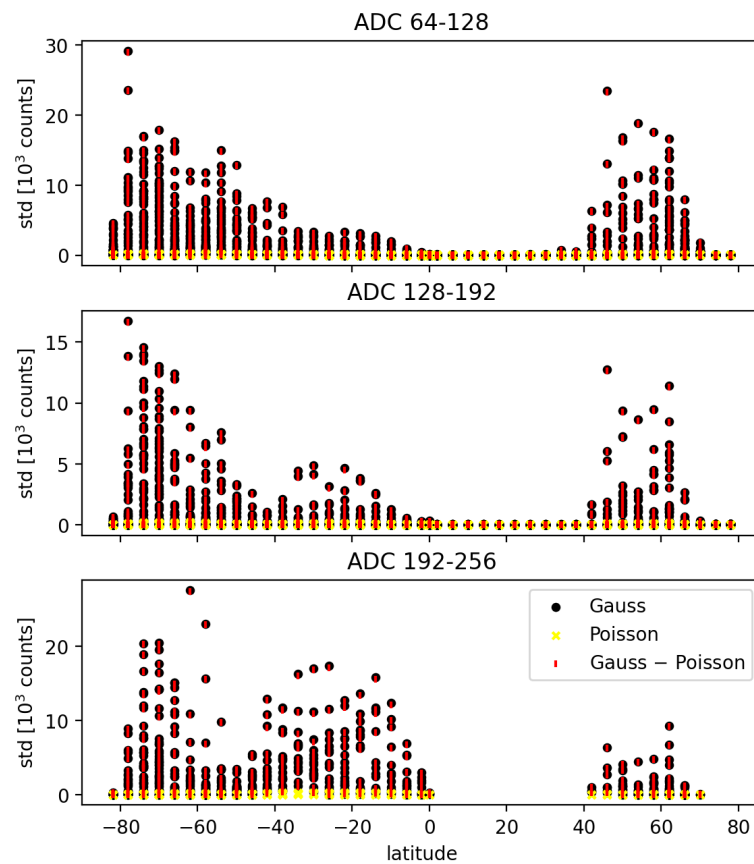


Figure 3.7: The standard deviation according to the Gaussian and Poisson distributions, and their difference, as a function of latitude. Each point represents one four-degree bin. All bins with $\lambda > 20$ are included.

3.3.1 Skewed distributions

To understand the real distribution of our data, we looked at histograms for all the bins which contain more than one hundred counts. Near the equator, the Gaussian distribution appears to be a good fit, however, as we get to higher latitudes, the histograms become more and more skewed. The fundamental skewed distribution, the skew-normal distribution, seems to work well in many situations but it fails in long-tailed cases, which occur in polar regions. Therefore, to find the best fit, we took the trial-and-error approach and tested all skewed probability distributions available in Python module *scipy.stats*.³

The two most suitable ones were found to be the exponentially modified Gaussian distribution and the Johnson SU distribution. Although the Johnson SU seemed to be handling the long tails slightly better, it failed in less dispersed data sets. Therefore, the former was used to get the mean and standard deviation of the background for events examined in Ch. 4. The detection significance in terms of the signal-to-noise ratio was then determined as

$$SNR = \frac{(\text{event count rate} - \text{background count rate})}{\sigma_{\text{bgd}}}. \quad (3.3)$$

Here, we present a few example histograms from different locations. Each figure consists of three subplots with an identical histogram but different distribution fit. From top to bottom, the subplots show the Gaussian ([scipy.stats.norm](#)), skew normal ([scipy.stats.skewnorm](#)), and the exponentially modified Gaussian ([scipy.stats.exponnorm](#)) fit. The energy band, central longitude and latitude of the four-degree bin, and the number of data points N within the bin are specified at the top of each figure.

Fig. 3.8 is an example from equatorial region, shown only in the two lower energy bands because nothing was detected in the highest one. As expected, the distributions are very close to Gaussian, meaning that the background here does not fluctuate or show much variability with time. Another example from a region close to the equator is from the area between the SAA and the north polar ring (Fig. 3.9). The highest energy band is again not shown due to zero counts detected. In contrast to Fig. 3.8, the distributions are not Gaussian but show two distinct peaks. Note, that these histograms are from the region of elevated background in the interpolated map, shown in Fig. 3.6 and discussed in Sec. 4.4.

The northern polar ring region is displayed in Fig. 3.10. The lowest and highest energy bands exhibit a long-tailed distributions, while the middle energy band resembles the Gaussian. This inconsistency illustrates the high dynamics of the region.

The last example is from a near-limb SAA region, shown in Fig. 3.11. In all three energy bands, the distribution is skewed to the right. Note, that the count rate is much higher in the highest energy band. This agrees with our conclusions from Sec. 3.1.1 and 3.1.2 that the SAA region is dominated by the most energetic particles.

³<https://docs.scipy.org/doc/scipy/reference/stats.html#module-scipy.stats>

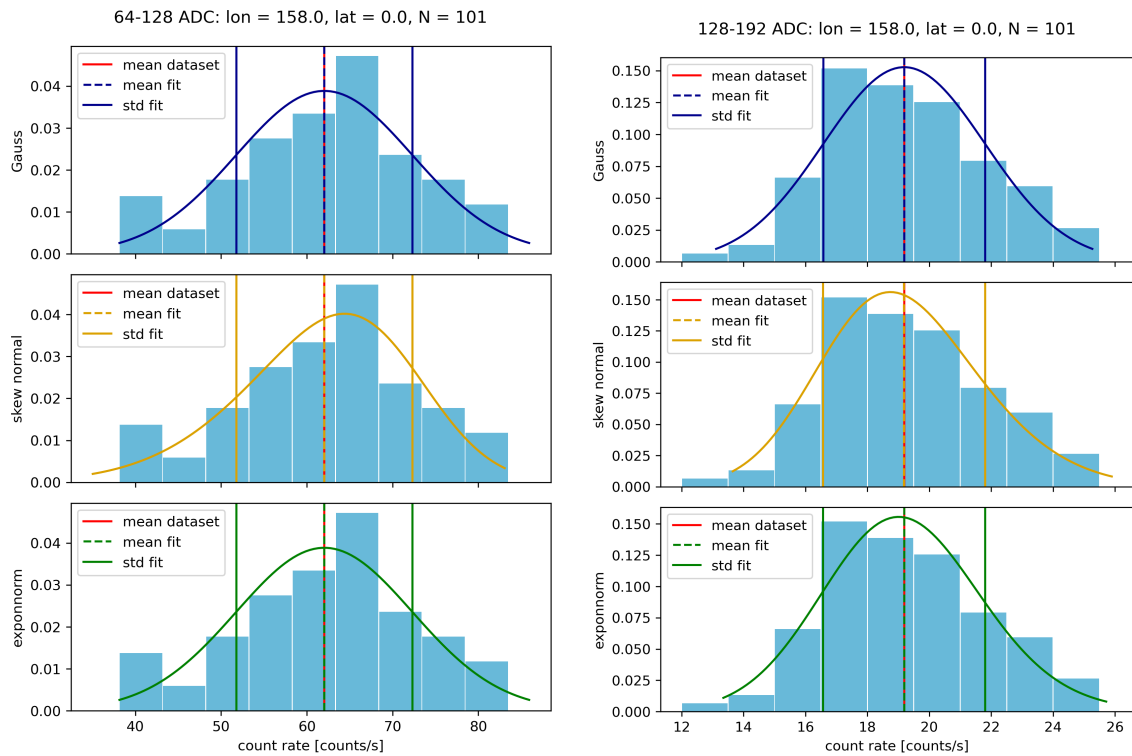


Figure 3.8: An example of histograms for equatorial region. See text for more details.

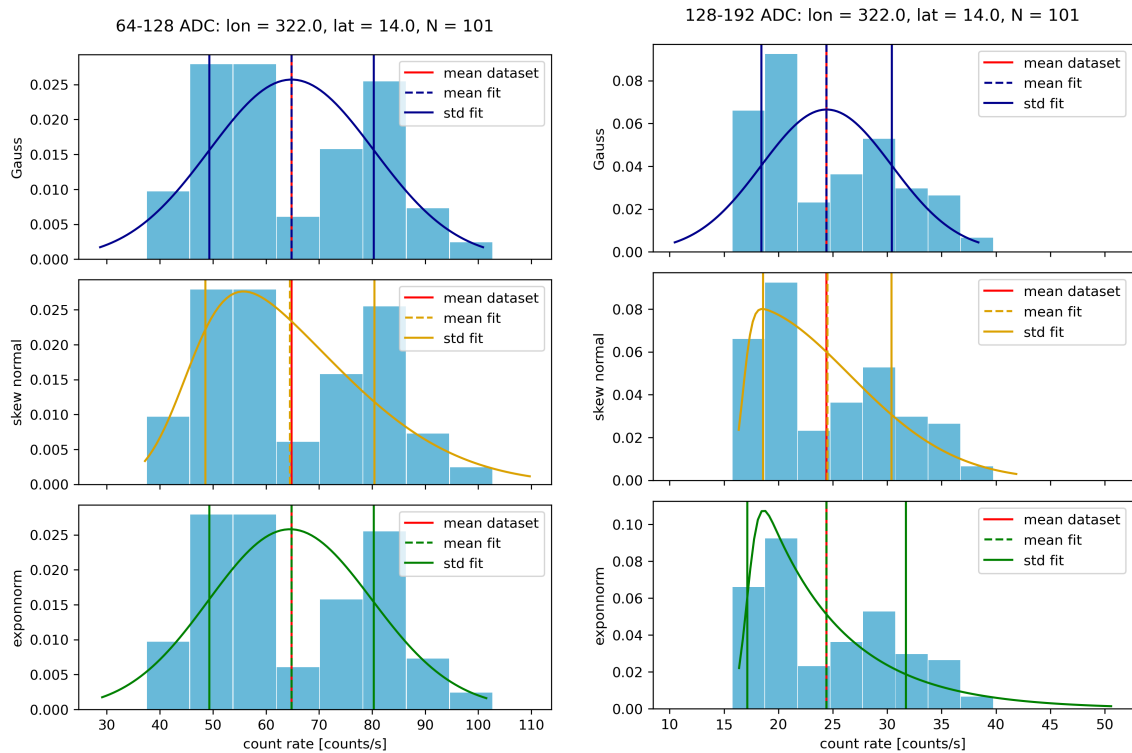


Figure 3.9: An example of histograms from region between the SAA and the north pole. See text for more details.

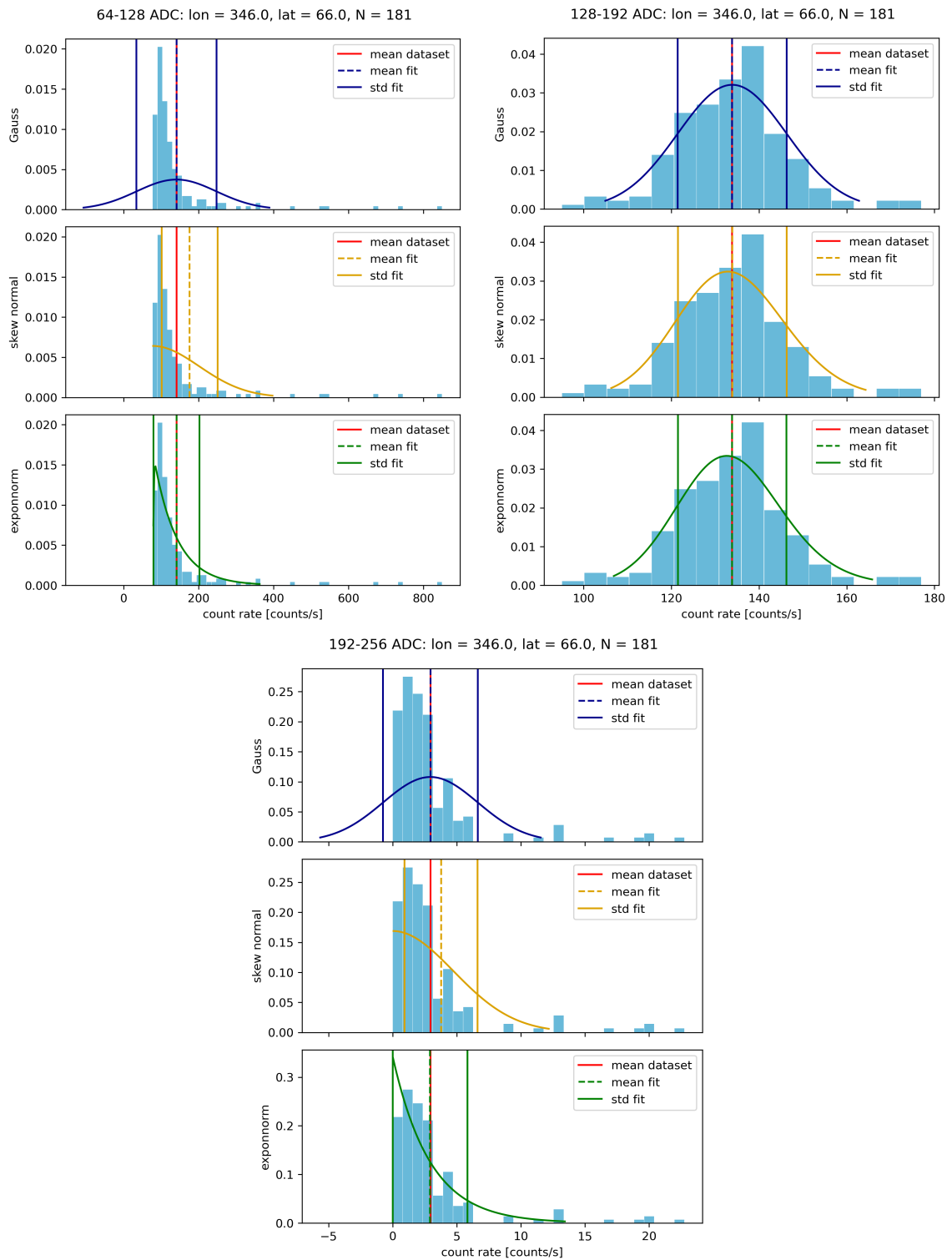


Figure 3.10: An example of histograms from the north polar region. See text for more details.

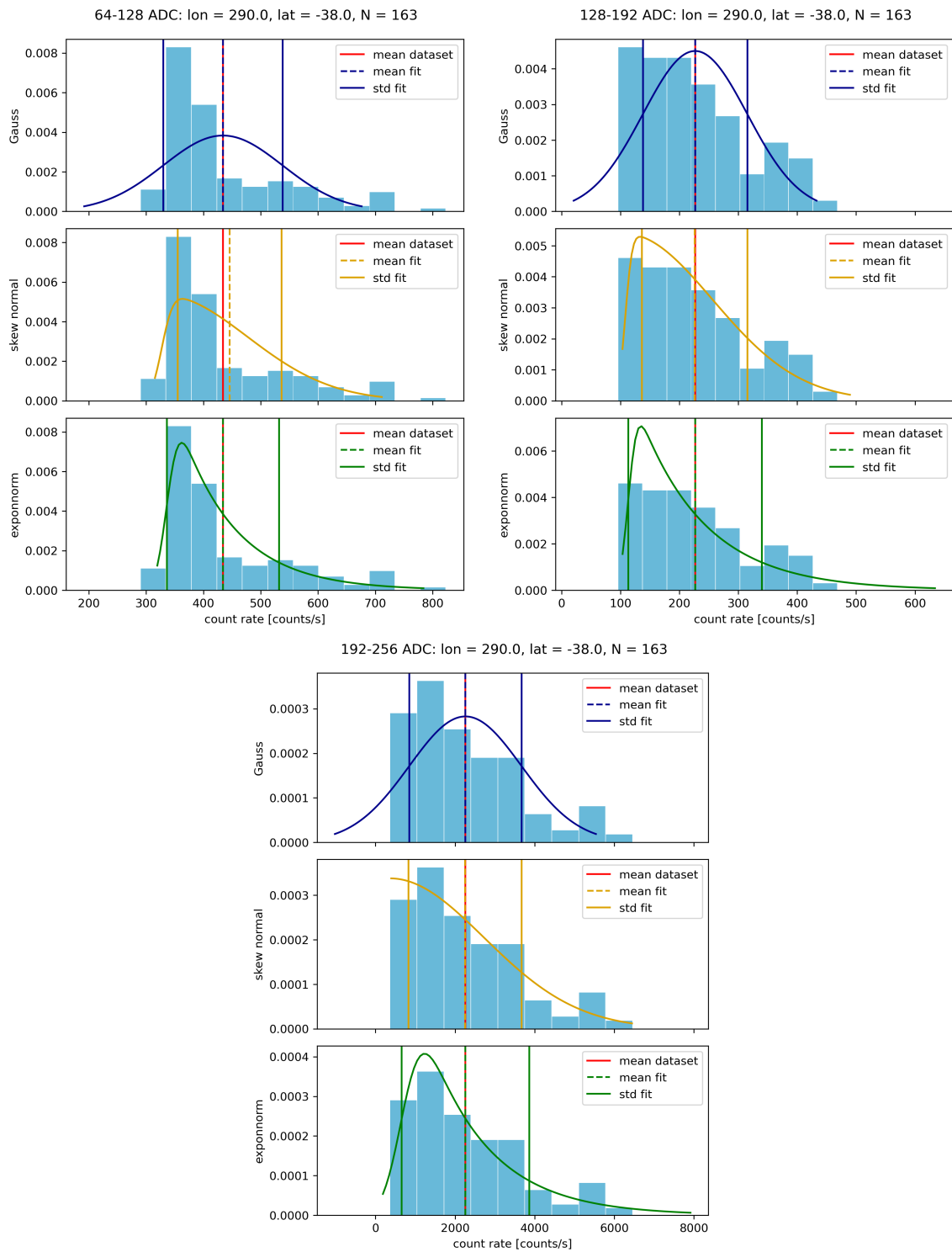


Figure 3.11: An example of histograms from the SAA region, close to its limb. See text for more details.

Chapter 4

Results and discussion

4.1 Radiation belt enhancements in April 2021

4.1.1 Event overview

Two radiation belt enhancements from April 2021 are examined in this section. The first one began on April 17 when the 10^3 pfu threshold for GOES electron flux was exceeded at 16:35, and remained elevated until April 25 with maximum of nearly 20 000 pfu at 16:05 on April 23. This RBE was initiated by an HSS detected at Lagrange point L1 by DSCOVR at 07:09 on April 16, and enhanced by another HSS at 00:07 on April 17. Both HSSs were linked with an interplanetary shock observed at 14:43 on April 16. The solar wind speed at L1 was above 500 km s^{-1} between April 17 and April 21, with a maximum of 696.0 km s^{-1} on April 19. The Kp index was slightly higher during this RBE event and reached index 5 several times between April 16 and 25.¹

The second RBE was initiated by an HSS detected at 20:55 on April 23 with a peak solar wind speed of 538.0 km s^{-1} on April 27. A CME-driven interplanetary shock, detected by DSCOVR at 22:24 on April 24, might have also contributed to the particle acceleration. The GOES electron flux began increasing at 11:30 on April 27, exceeded the RBE threshold at 18:20 the next day, and remained elevated until May 2. Compared to the first RBE, this one was considerably weaker with maximum electron flux approximately 1800 pfu at 18:00 on April 30. The geomagnetic activity was low with maximum Kp = 3 during the entire event.²

The GOES proton flux was at background levels during the entire month of April. Four solar flares erupted during the second half of April 2021, the strongest one being an M1.1 class flare on April 19. No impacts related to any of them were reported.

4.1.2 GRBAlpha observations

In April 2021, GRBAlpha was primarily mapping the LEO background with various exposure times, as previously discussed in Sec. 3.1. Measurements were taken every day between April 14 and 20, on 22, and during the night from 27 to 28. However, two longer

¹Space weather conditions during the first RBE event can be reviewed at [this iSWA layout](#).

²Space weather conditions during the second RBE event can be reviewed at [this iSWA layout](#).

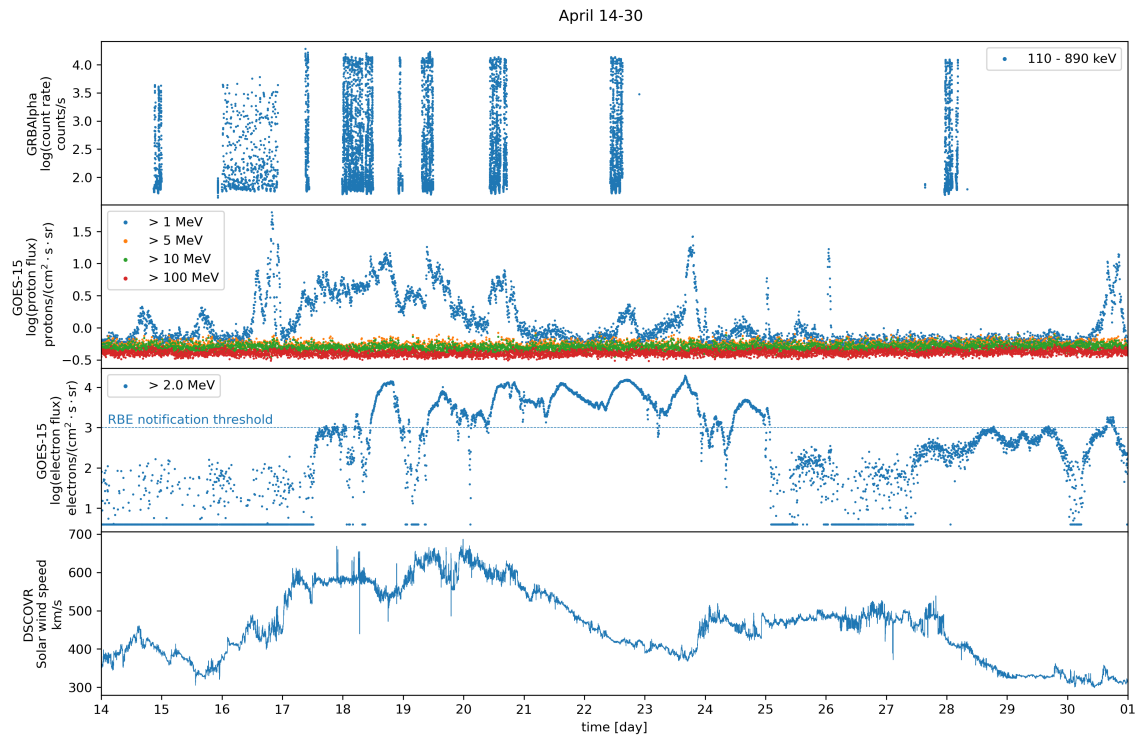


Figure 4.1: *Top to bottom:* GRBAAlpha observations, proton and electron flux measured by GOES, and the solar wind speed by DSCOVR. The second half of April 2021 is shown. The dashed horizontal line in the plot for electron flux marks the NASA/NOAA threshold for RBE events.

measurements with 120 s exposures are only available in the lowest energy band. These measurements were taken on April 15 and 16 and contain most of the data from the quiet period prior to the RBE events. All April data for the lowest energy band are displayed in Fig. 4.2, separately for the first quiet days and during the two RBEs. Undoubtedly, the count rate observed during the RBE events is highly elevated, especially in the polar rings.

In further analysis, data from both RBEs are examined together. The residuals are presented in Fig. 4.3 and the SNR values in Fig. 4.4. All of these maps show the wavy pattern of polar rings but the SAA is not distinguishable in any of them. The SNR maps for the lowest and highest energies also contain some indications of the secondary rings while no similar features are observed in the middle energies. Moreover, the SNR map in the lowest energy band contains few additional artifacts near equatorial regions, however, these are likely caused by the imperfect background model or small amount of data points within the four-degree bins.

Tab. 4.1 summarizes the peak SNR values for each energy band, along with the time and location when they were reached. All of them come from the regions of polar rings and were observed on April 19, when the solar wind speed was at its highest levels.

Table 4.1: The maximum SNR values, times when they were reached and location of GRBAAlpha at the time of measurement.

E [keV]	max(SNR)	time	longitude	latitude
~ 110 to ~ 370	530	2021-04-19 10:35:16	342.5	71.8
~ 370 to ~ 630	2468	2021-04-19 08:24:28	50.9	-57.7
~ 630 to ~ 890	4769	2021-04-19 08:24:28	50.9	-57.7

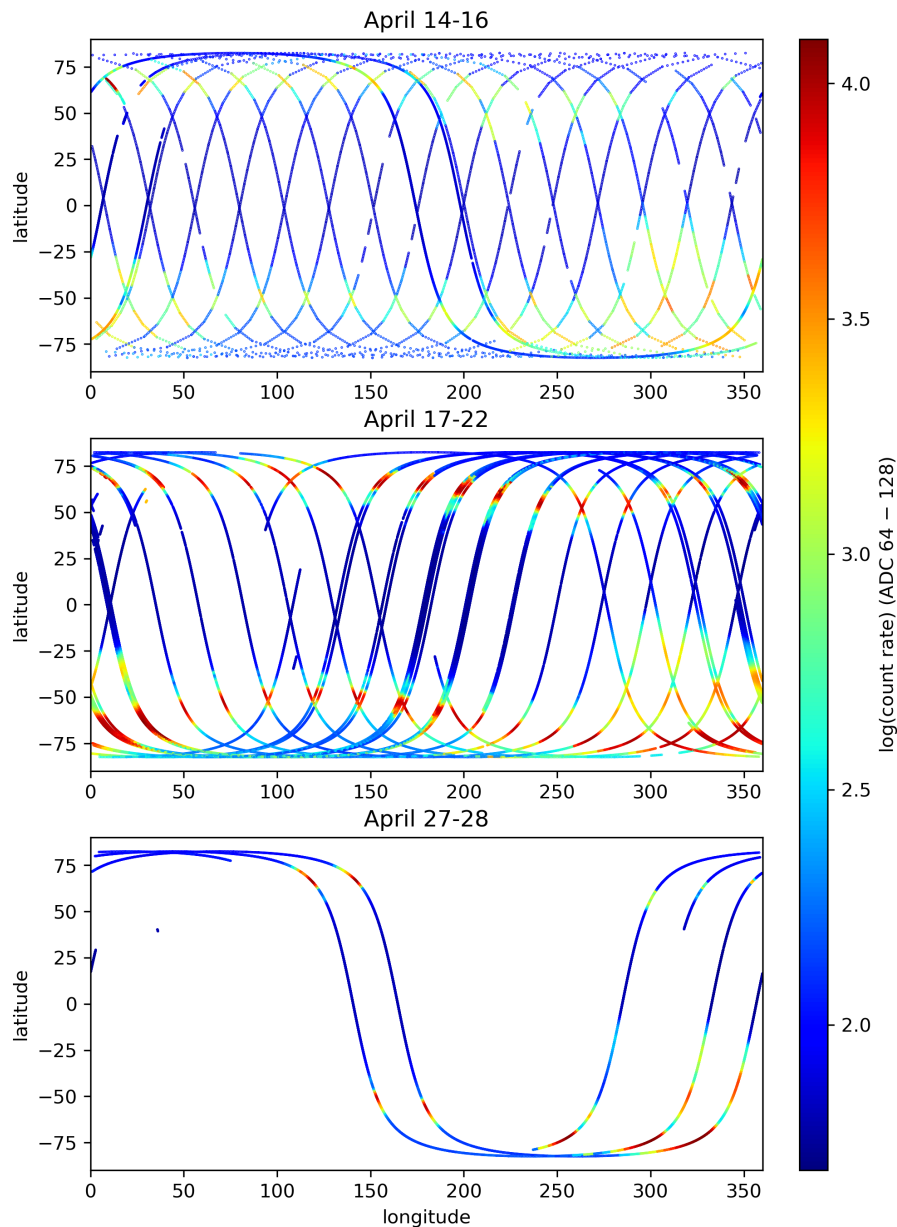


Figure 4.2: Ground tracks of April data revealing the difference in count rate during quiet times and RBE events. The maps are shown in the lowest energy band $\sim 110 < E$ [keV] $< \sim 370$.

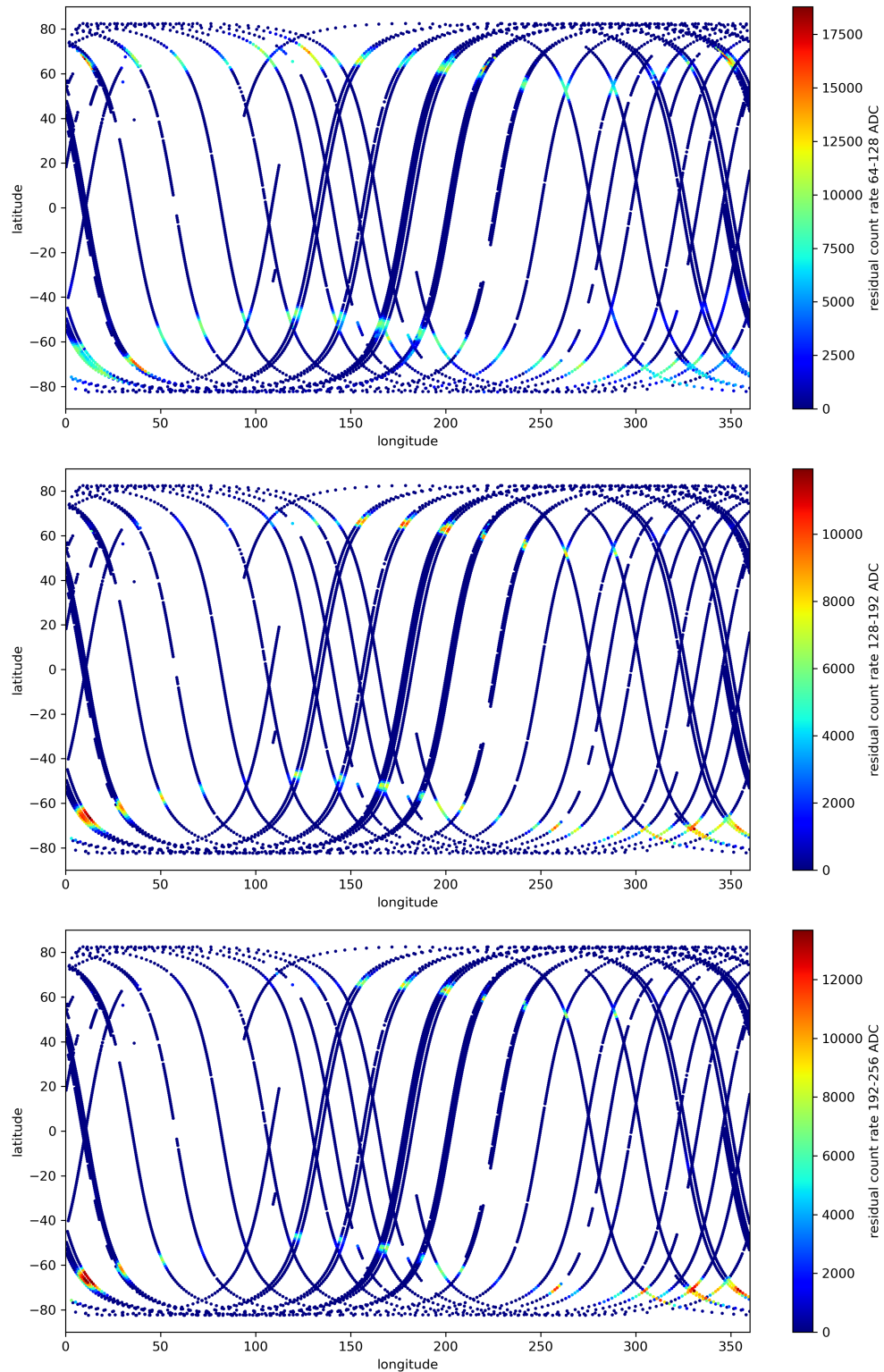


Figure 4.3: Ground tracks of GRBAAlpha during April RBEs with residual count rate shown in color. *Top:* $\sim 110 < E \text{ [keV]} < \sim 37$. *Middle:* $\sim 370 < E \text{ [keV]} < \sim 630$. *Bottom:* $\sim 630 < E \text{ [keV]} < \sim 890$.

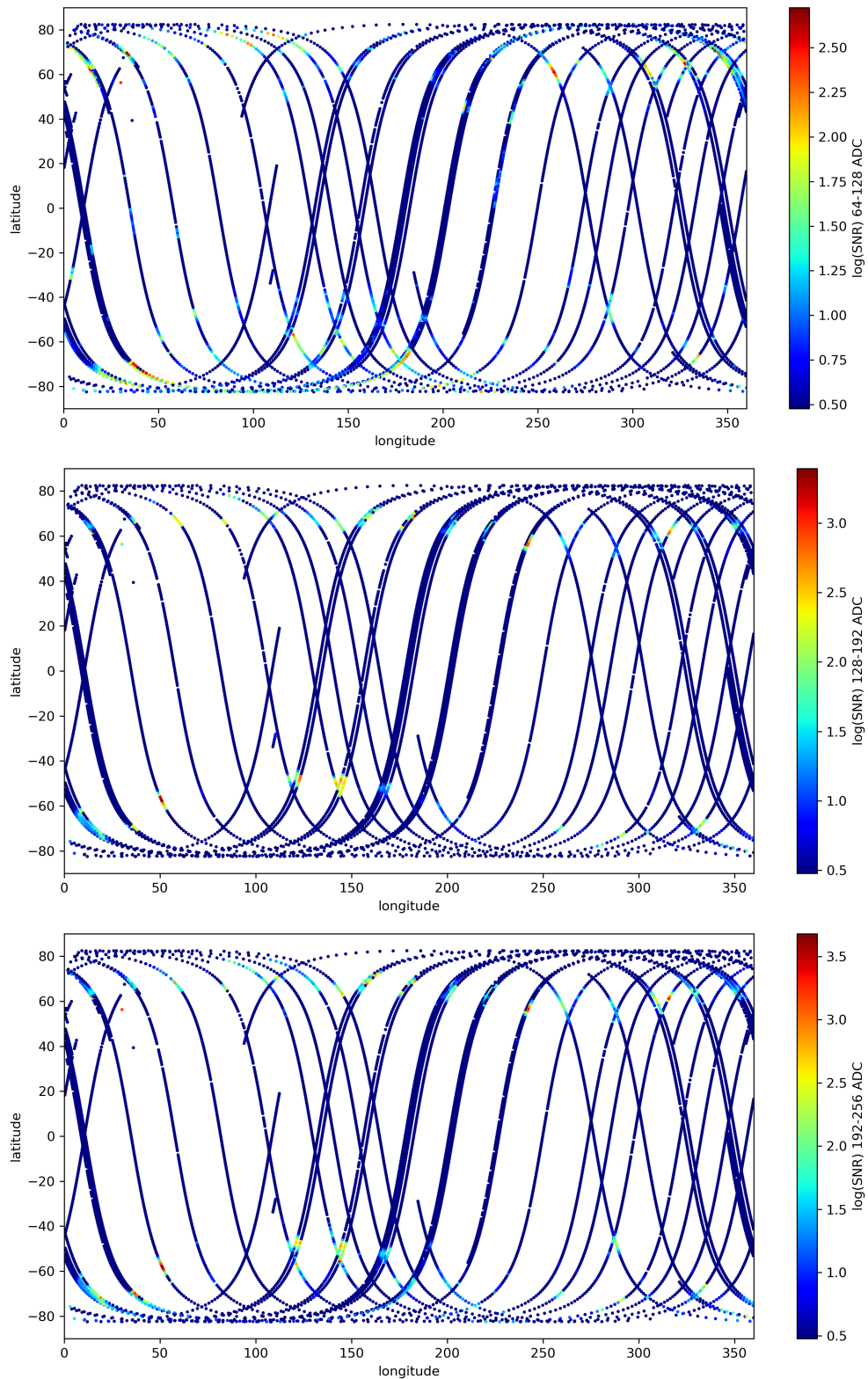


Figure 4.4: Ground tracks of GRBAAlpha during April RBEs with a logarithm of SNR values shown in color. The lower color bar limit is set to 3σ . *Top:* $\sim 110 < E \text{ [keV]} < \sim 37$. *Middle:* $\sim 370 < E \text{ [keV]} < \sim 630$. *Bottom:* $\sim 630 < E \text{ [keV]} < \sim 890$.

4.2 Solar energetic particle event on October 28, 2021

4.2.1 Event overview

On October 28, the GOES proton flux for $E > 100$ MeV exceeded the SEP threshold of 1 pfu at 16:35, stayed above the threshold level until 4:00 on October 30, and returned to its background values one day later. The 10 pfu threshold for $E > 10$ MeV was exceeded at 17:40 on October 28, dropped below the threshold on October 30 at 14:00, and remained elevated until November 4. The GOES electron flux for $E > 2$ MeV was slightly elevated between 16:00 on October 28 and 4:00 on October 29. Geomagnetic activity was low with maximum $K_p = 2$ until October 30.

This SEP event was directly linked to an X1.0 solar flare and O-type CME. The flare began at 15:17, peaked at 15:35 and lasted for about 30 minutes. The CME erupted from the same active region at 15:53 with estimated speed of 1109 km s^{-1} . Proton flux in both energies began increasing around 16:05, about 30 minutes after the flare's peak and 12 minutes after the CME eruption. On October 29, an M1.5 flare erupted at 2:22 with no events associated.

According to NOAA space weather scales³, an X1.0 flare can cause a strong (R3) radio blackout storm, during which a loss of VHF radio communication is possible. The SEP event was ranked as a minor (S1) solar radiation storm, which can increase VHF radio disruptions in polar regions.

In the preceding week, the solar activity was moderate with no Earth-directed CMEs and four M-class flares, none of which triggered further events. Both proton and electron fluxes at GOES were at background levels, and the K_p index reached 2 at maximum. Therefore, all magnetospheric disturbances after the flare eruption are considered to be related to the described SEP event.⁴

4.2.2 GRBAAlpha observations

On October 28, GRBAAlpha took seven separate measurements throughout the day. Five of them were taken before the flare eruption, between 4:30 and 13:20. Each of these five measurements lasted only five to eight minutes and were therefore left out of the analysis. The last measurement of the day is from 17:35 to 17:40 and was also left out because of its short duration.

The longest observation, analysed in this section and displayed in the top plots of Fig. 4.5, was taken between 14:24 and 16:45. During this period, the satellite entered the SAA from the south, continued towards the north pole, crossed the equator on its way to the south pole, and passed the SAA and the north pole once more. The solar flare erupted after GRBAAlpha left the north polar ring the first time.

South polar ring

GRBAAlpha passed the south pole between the flare eruption and the SEP arrival at GOES. Therefore, we do not expect strong space weather effects in this part of the orbit. During

³<https://www.swpc.noaa.gov/noaa-scales-explanation>

⁴Space weather conditions can be reviewed at [iSWA](#).

the entry and exit phase, the residual plot shows some variability, what suggests that the ring was slightly displaced, but the SNR stays at relatively low level throughout the entire SP pass (Tab. 4.2).

It is worth noting that the residuals highly fluctuate also during the first SAA and NP passes, which could be considered as a part of the background model. However, the SNR is not significantly increased in these regions what means that the standard deviation here is high. Therefore, these fluctuations most likely result from our background model, which is static, while the real LEO environment in polar and SAA regions is very dynamic also during quiet space weather conditions.

Table 4.2: The maximum SNR values during the entry and exit phase of the south polar pass.

E [keV]	SP entry		SP exit	
	max(SNR)	time	max(SNR)	time
~ 110 to ~ 370	0.1	15:38:42	1.9	15:54:22
~ 370 to ~ 630	7.4	15:38:46	6.0	15:53:10
~ 630 to ~ 890	8.8	15:38:46	7.2	15:53:14

South Atlantic Anomaly

The first SAA pass was longer and higher number of counts was detected because the satellite crossed a more central region, in contrast to the second pass which was over the western limb. During the second pass, there is a bit steeper increase in both the count rate and residual count rate data, for all three energy bands starting approximately at 16:04:30, around the same time as the SEPs arrived at GOES. Therefore, this could be the SEP arrival detected by GRBA α . However, the SNR reached only 3 in the lowest energy band and 4 in the two higher ones so this feature can be just a result of the SAA's asymmetry, especially near its limbs.

North polar ring

A comparison of the two passes over the north pole, before and after the eruption, shows strongly increased count rate in all energy bands, most striking in the highest one. Average count rates from inside of the ring are reviewed in Tab. 4.3. Note the ratio for the highest energy band which reaches 30. This reveals an intense particle injection into magnetosphere via the northern polar cusp.

Table 4.3: A comparison of average count rates during two passes over the north pole, before the SEP event (NP₁) and during its onset (NP₂).

E [keV]	NP ₁ [cps]	NP ₂ [cps]	NP ₂ /NP ₁ [cps]
~ 110 to ~ 370	100 ± 8	230 ± 2.3	2.3 ± 0.5
~ 370 to ~ 630	139 ± 8	340 ± 2.4	2.4 ± 0.2
~ 630 to ~ 890	2.2 ± 0.8	70 ± 20	30 ± 15

In the residual plot, we observe a peak during the second entry phase. This peak is followed by a dip in the lowest energy band but not in the two higher ones. This indicates

that the lowest energetic particles were mostly shifted to lower latitudes while the ring expanded for the more energetic ones.

The residuals begin to increase at 16:26:00 when the satellite was at 46.31 degrees of latitude. The observation ends during the exit phase and therefore it is not possible to estimate the expansion in this direction. During the entry phase, the SNR reached 4, 91, and 111 for the lowest, middle, and highest energy band, respectively. Maximum SNR values during the entire pass over the north pole and the times when they were reached are in Tab. 4.4. As suspected from the count rate ratios in Tab. 4.3, the SNR values confirm that this SEP event strongly affected the most energetic particles.

Table 4.4: The maximum SNR values during different parts of the NP pass.

E [keV]	NP entry		NP overall	
	max(SNR)	time	max(SNR)	time
~ 110 to ~ 370	4	16:26:46	55	16:36:42
~ 370 to ~ 630	91	16:26:38	99	16:38:50
~ 630 to ~ 890	111	16:26:42	468	16:30:50

4.2.3 VHF radio loss

On October 29, GRBAlpha experienced an unusual situation. The battery voltage decreased from 8.16 V at 01:09 to 6.80 V at 21:56. The GPS and OBC temperatures increased to 47 °C at 12:02, and the COM temperature to 31 °C at 8:48.

At the time when these problems began, the satellite crossed the SAA as demonstrated in bottom left part of Fig 4.5. The proton flux was still above the threshold for both energy bands. An M1.5 flare erupted during this period, however as noted earlier, this flare has no further recorded space weather impacts.

At 23:00, the temperatures were back at normal values and communication via VHF radio worked. Since the following pass at 00:36 on October 30, there has been no response from the satellite and uplink communication had to be switched to UHF radio. During the orbit between these two passes over the ground station, GRBAlpha crossed the SAA, as shown in bottom right part of Fig. 4.5. Soon after this SAA pass, the last sunsensor data was received.

Looking at the entire series of events, it is highly probable that the VHF radio loss was caused by the aforementioned SEP event. Although we do not have measurements from the exact time when the damage happened, the GOES proton flux in three lower energy bands was much higher than during the detected enhancement at the onset of the SEP event, and at about the same level in the highest band. Therefore, it is likely that denser particle population in polar regions and the SAA lasted for the entire period, and the satellite had been accumulating energy for more than a day. Eventually, as GRBAlpha was not in a safety mode, this might had lead to the radio loss.

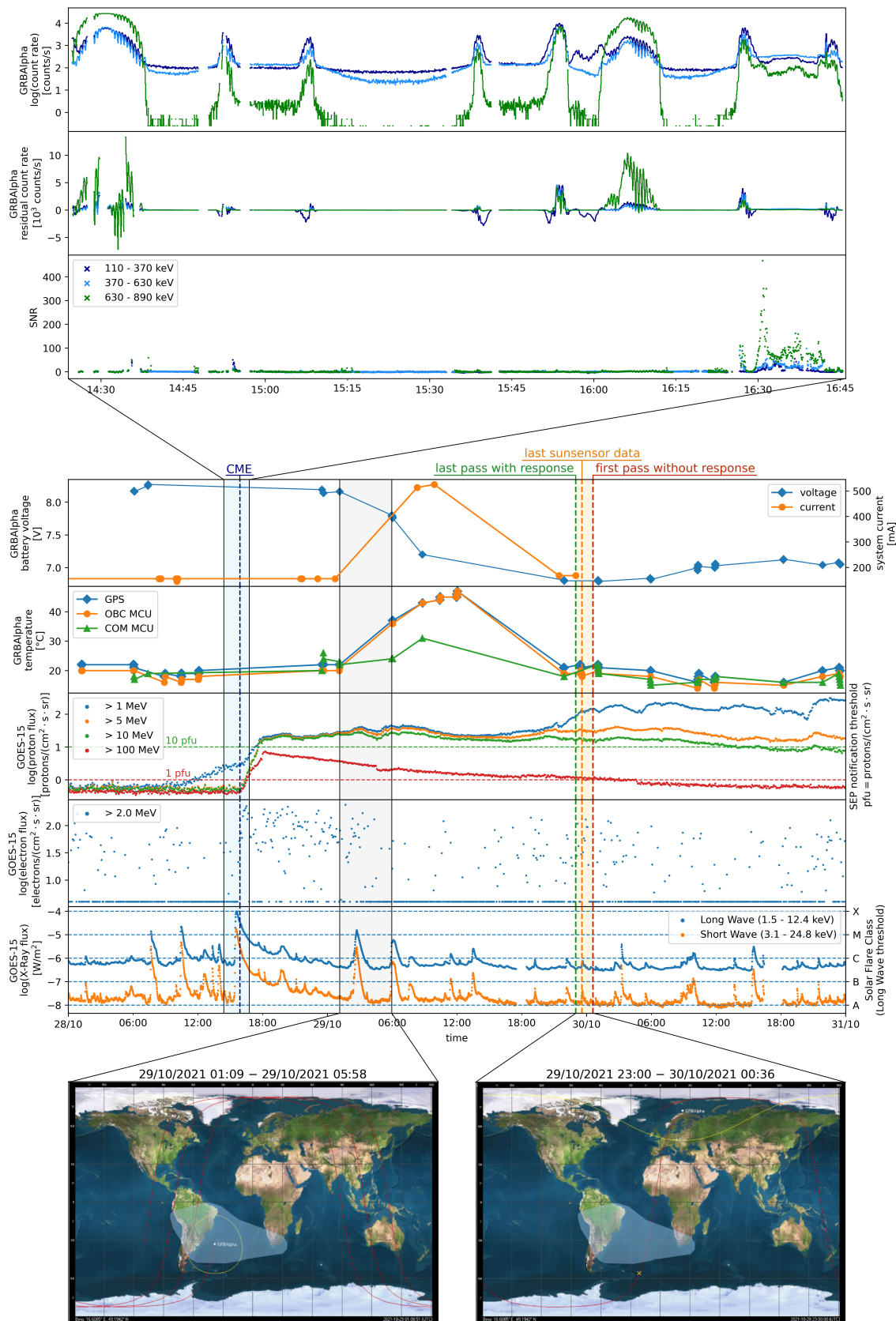


Figure 4.5

Figure 4.5 (previous page): A timeline of events which happened from October 28 to 30, 2021. *Top:* GRBAlpha count rate and residual data, and the SNR values during the onset of the SEP event. *Middle:* GRBAlpha housekeeping data and GOES proton, electron, and X-ray flux. The green and red horizontal lines in proton flux data mark the thresholds for an SEP event. The blue horizontal lines in X-ray flux data show the solar flare classes. *Vertical lines:* CME eruption time (blue), time of last received sunsensor data (yellow), last pass with (green) and first pass without (red) satellite response above the ground station. *Bottom:* Ground tracks (red curves) of GRBAlpha during the period when the battery voltage began to decrease (left) and when the VHF radio was damaged (right). The shaded area shows an approximate SAA region. The yellow cross in the right map marks GRBAlpha location when the last sunsensor data were received. The maps were obtained from the [Orbitron](#) app.

4.3 Geomagnetic storm on March 13, 2022

4.3.1 Event overview

On March 13, the K_p index jumped from 0 at 9:00 to 6 at 15:00, and stayed elevated until 6:00 the next day. This geomagnetic storm was caused by a CME-driven interplanetary shock which was detected at L1 by DSCOVR at 10:11. The IMF, observed by ACE and DSCOVR at L1, was oriented southward in periods from 10:30 to 14:00, 15:30 to 17:00, and 21:00 to 22:30. The GOES proton flux in $E > 1$ MeV increased at 10:45 and the electron flux was slightly elevated between 13:00 and 16:30. The initial CME erupted on March 10 and was classified as a C-type CME with an estimated speed of 677 km s^{-1} .⁵

The $K_p = 6$ is considered to be a moderate (G2) geomagnetic storm which may disturb electric systems and high-frequency radio propagation in higher latitudes, and the auroral oval can move to 55 degrees of geomagnetic latitude. During the night from March 13 to 14, the aurora was also observed from Czech republic at around 50 degrees of magnetic latitude.⁶

4.3.2 GRBAlpha observations

GRBAlpha took measurements from 23:35 on March 13 to 00:10 on March 14. During this period, the K_p index was still at 6, the electron flux was back at background values, and the proton flux had recovered from the initial increase, however, there was another slight enhancement during the measurement. The observation began during an exit from the southern ring and ended after the satellite entered the northern ring.

In both regions we observe double structures in the lowest and highest energy bands. The middle one does not seem to be affected. Its residuals are close to zero at all times, except for a small decrease in the northern ring, and the SNR is within 3σ throughout the entire observation.

Undoubtedly, the lowest energy band experiences the strongest disturbances. The intensity of the northern secondary ring is at nearly the same level as the primary one. The SNR reaches a maximum of 1692 at its peak and stays elevated within the primary

⁵Space weather conditions can be reviewed at [iSWA](#).

⁶<http://ukazy.astro.cz/prirustky.php?Id=10167>

ring. The southern secondary ring for this energy band is also slightly enhanced with SNR reaching 45. The residual plot for highest energies does not indicate too much changes, however, the SNR is increased in both polar regions, reaching maximum of 444 in the northern secondary ring. Tab. 4.5 reviews the maximum SNR values in different regions of this orbit.

After the SP exit, the residuals return to background values at 23:41:24 which corresponds to latitude of -36.5 degrees. The increase at the NP entry phase begins at 00:02:32 and 42.5 degrees of latitude.

Table 4.5: The maximum SNR values in different parts of the orbit during a geomagnetic storm.

E [keV]	secondary SP ring		secondary NP ring		primary NP ring	
	max(SNR)	time	max(SNR)	time	max(SNR)	time
~ 110 to ~ 370	45	23:39:26	1692	00:04:46	89	00:07:34
~ 370 to ~ 630	0.6	23:38:10	1.7	00:01:14	-0.9	00:08:30
~ 630 to ~ 890	28	23:40:50	444	00:05:46	27	00:07:06

4.3.3 VZLUSAT-2 observations

Although the VZLUSAT-2 data were primarily used to fill in some background gaps and they were not analysed into depth, it is worth noting, that they contain the secondary rings even one week after this geomagnetic storm.

Fig. 4.7 displays measurements taken on March 19 and 20. The GOES proton and electron fluxes were at background levels, and $K_p = 3$ at maximum during the entire week between this observation and the examined geomagnetic storm.⁷ Both secondary rings are evident in the lowest energies, and weakly also in the highest ones. This illustrates the long-term impacts of geomagnetic storms on the LEO environment which we did not consider in our background model.

As the GOES fluxes and K_p index were below our background conditions throughout the most part of this measurement, these data are included in our background model even though they evidently contain features related to space weather events. This implies that in future analysis, the background conditions will have to be modified to account for these long-term effects.

⁷Space weather data can be reviewed at [iSWA](#).

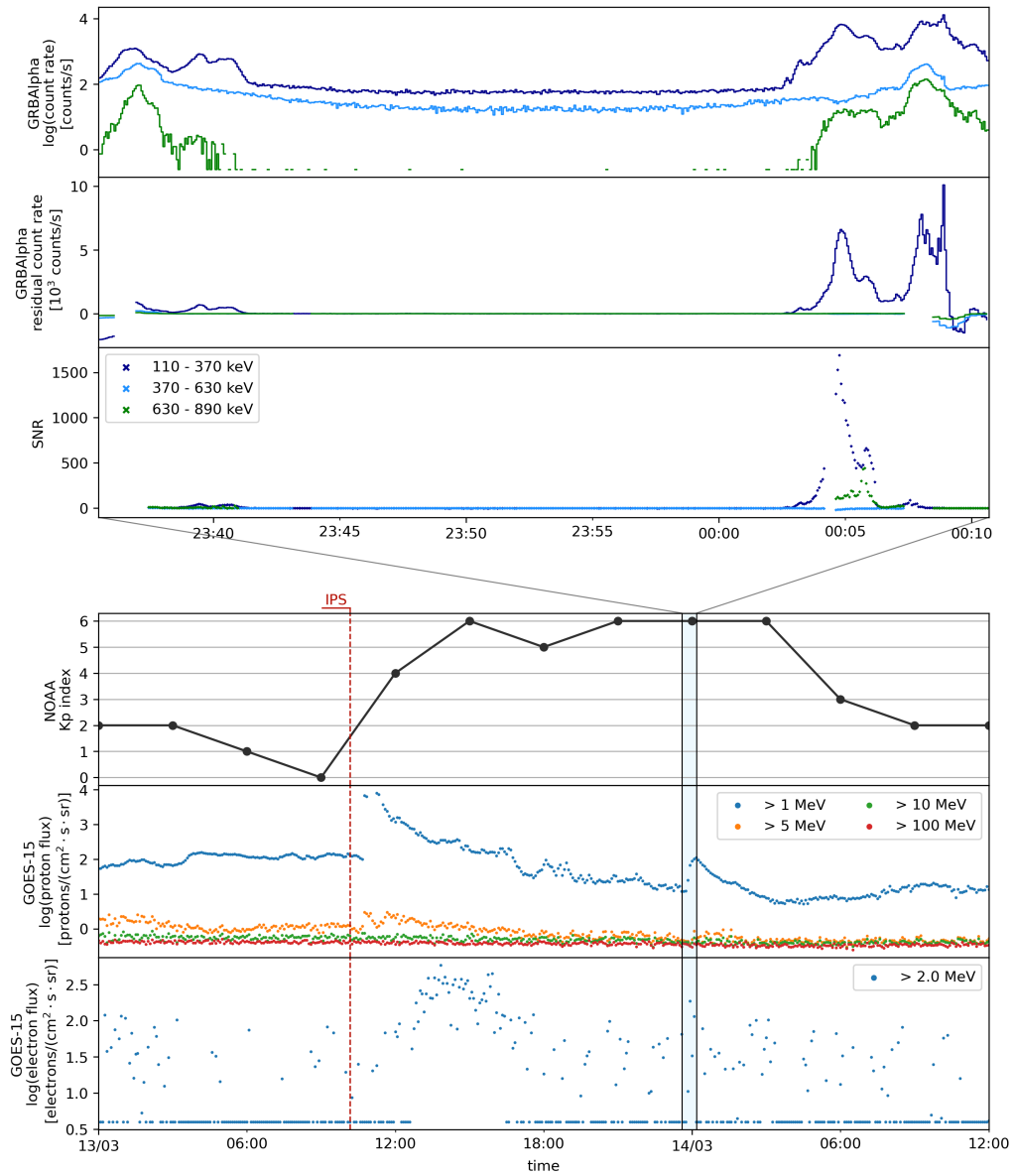


Figure 4.6: *Top:* GRBAAlpha count rate and residual data, and their corresponding SNR values. *Bottom:* The Kp index and GOES proton and electron flux. The red vertical line marks the time of the interplanetary shock arrival at L1, as detected by DSCOVR.

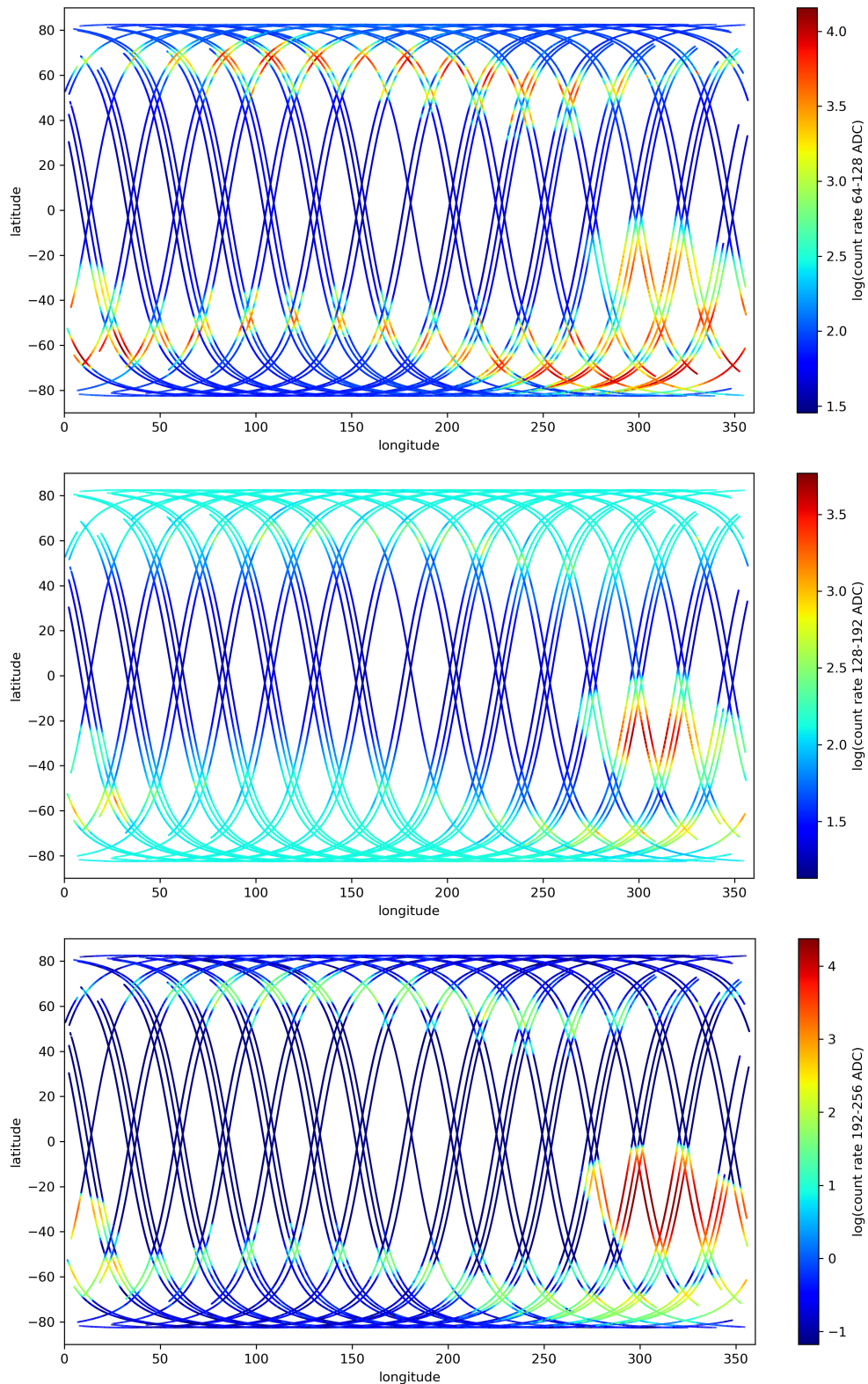


Figure 4.7: Ground tracks of VZLUSAT-2 during observation from March 19 to 20 with count rate data shown in color. Note the secondary rings present in the lowest (top) and slightly in the highest (bottom) energy bands.

4.4 Elevated count rate between the SAA and north polar ring

As mentioned in Sec. 3.2.2, while trying to establish a background model by interpolating the data from times of quiet space weather conditions, we spotted an increased count rate in the region between the SAA and the north polar ring. Fig. 3.6 shows the interpolation done for the middle energy band.

To try to understand the nature of this anomaly, we looked separately at orbits when GRBAlpha was going northward and southward, and we found that the increased count rate was only present in times when the satellite was headed from the SAA towards the north pole. Fig. 4.8 and 4.9 display the ground tracks separately for each direction. This suggests that the SAA is the key contributor to this feature.

One hypothesis is that the enhanced flux of high energy particles, especially protons, in the SAA induces nuclear reactions in the satellite's components, and as the produced radioisotopes decay, their products are detected resulting in an increased count rate. As we do not have information about the type of incident particles, it is challenging to determine the exact process. However, various simulations are ongoing in order to learn more about this anomalous region.

From the data processing point of view, this short-term activation contributes to instrumental noise in the data. Histograms from this location, demonstrated in Fig. 3.9, exhibit a double peak structure, even though we would expect a rather Gaussian character as they are from near-equatorial region. The count rate ratio of the two peaks is approximately 1.5 and 1.4 for the lowest and middle energetic bands, respectively. In the highest energies, the count rate was zero. As we did not consider this feature in our background model, the measurements from this region may seem slightly more statistically significant. Therefore in future analysis, two background models should be established to avoid misinterpreting of the data.

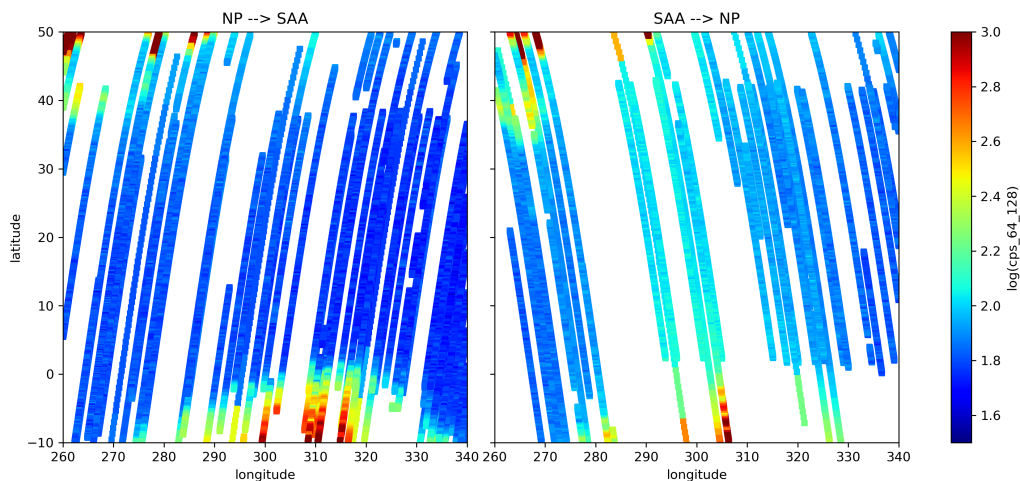


Figure 4.8: Map of southward (left) and northward (right) ground tracks of GRBAlpha, zoomed into the region between the SAA and north polar ring. Count rate data for $\sim 110 < E [\text{keV}] < \sim 370$ are shown in color.

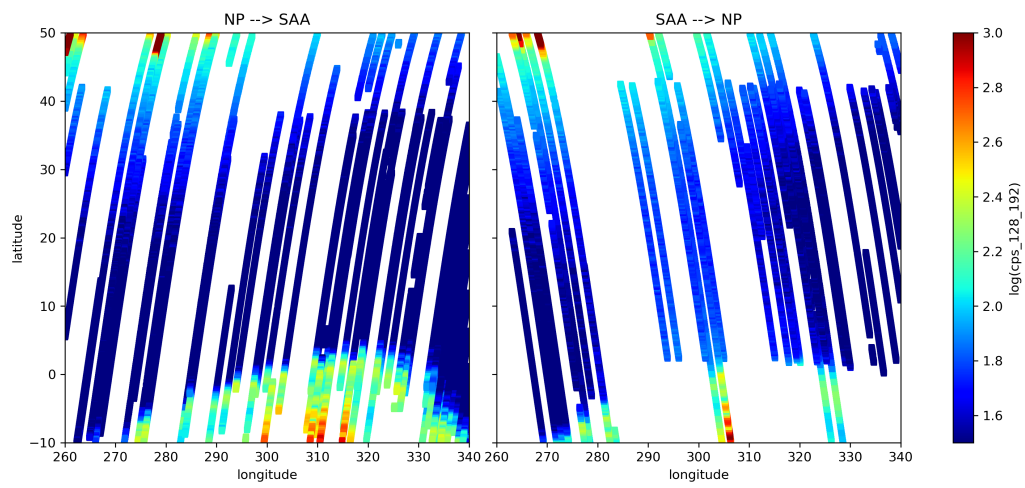


Figure 4.9: The same as Fig. 4.8 but with count rate data for $\sim 370 < E \text{ [keV]} < \sim 630$.

Conclusion and future insights

The aim of this work was to investigate space weather effects at the LEO environment observed by GRBAAlpha. We examined two radiation belt enhancements from April 2021 (Sec. 4.1), one solar energetic particle event from October 2021 (Sec. 4.2), and one geomagnetic storm from March 2022 (Sec. 4.3). In case of the SEP event and the geomagnetic storm, these were the only events of each type observed by GRBAAlpha.

RBEs, by definition, are enhancements of electron flux within the Van Allen belts. Our analysis has confirmed that their impact at LEO is concentrated in the regions of polar rings, especially the primary one which represents the outer radiation belt. The SNR values (Fig. 4.4) suggest some variability in the secondary ring as well but the residuals do not show high increase there. As expected, no effects on the SAA were observed.

The SEP event (Fig. 4.5) was found to affect mostly the regions inside of the polar rings. This makes sense as these solar particles arrive at relativistic speeds to the magnetosheath, from where they can directly access lower atmospheric regions via open magnetic field lines within polar cusps. The SEPs primarily contain protons and are known to enhance the flux within the SAA as well. This is not so obvious from our analysis. Although GRBAAlpha detected increased count rate in the SAA region at the time of the SEPs' arrival at GOES, the SNR from this time is between 3 and 4, which does not indicate too much of a significance. However, GRBAAlpha only observed the onset of this SEP event and as no other SEPs were detected throughout the year, so we cannot make any definite conclusions. The real SEP effects at LEO therefore remain unknown. Nevertheless, GRBAAlpha's VHF radio loss during this event implies that they are much more severe than what the measurement has shown.

The most characteristic LEO features for geomagnetic storms were found to be the secondary polar rings, very bright in the lowest and less intense in the highest energy band. The GRBAAlpha measurement (Fig. 4.6) does not include the SAA region, therefore we cannot conclude anything about the GST effects on the SAA. VZLUSAT-2 data (Fig. 4.7) taken one week after the event still exhibits the secondary rings which demonstrates the long-lasting effects of GSTs.

This long-term influence was not considered when developing our background model and the VZLUSAT-2 measurement shows that the established conditions did not cover them. This could be improved by using the K-indices instead, which correspond to specific locations on Earth. However, the K-indices are still just measures of the variations of the geomagnetic field, which means that when the field is enhanced for an extended period and the inner belt can be closer to the Earth, the Kp and K-indices can be low. Therefore, another indices, or perhaps the magnetic field strength itself, should be considered in future analysis.

The other two conditions used to characterize the LEO background are based on GOES proton and electron fluxes. As the GOES spacecraft orbits at GEO, its data are directly relevant only in the outer parts of the inner magnetosphere. Although they may be a good indicator of forthcoming disturbances, they do not reflect the current conditions at LEO nor they provide information on the long lasting LEO effects.

The LEO environment, especially the SAA and polar regions, is highly dynamic at all times. This can be seen in the top part of Fig. 4.5 where the residuals of the first SAA pass strongly fluctuate despite the fact that the solar activity was low during the entire preceding week. This shows that a static background model is not able to precisely describe the background conditions experienced by GRBAlpha and other LEO missions. Therefore, a more flexible model will have to be created, using real-time LEO data.

Moreover, there are additional factors with contributions to the background that cannot be neglected. Among them is the short-term activation of the satellite after passing the SAA, discussed in Sec. 4.4, but possibly also other, yet unmentioned, aspects such as the satellite's rotation which is not fully understood yet, or its altitude which, although does not vary drastically, can, in principle, play a role in such a dynamic environment.

The analysis has also revealed a few features which are worth exploring further. One of them is the fact that the secondary rings were never observed in the middle energy band, while in the lower and higher bands they often are present. Another remark is the bad communication with the satellite. Although this can be connected to the VHF radio loss, there might also be a correlation with ionospheric disturbances induced by solar activity.

Many different approaches can be taken to get new perspective of the data and LEO particle environment, such as:

- transforming the data into magnetic coordinates could provide better understanding of the boundary variations of the polar rings which are difficult to estimate when working in geographical coordinates,
- as the satellite orbits at SSO, meaning it passes a specific location on Earth always at the same local mean solar time, a relationship between the count rate and the local mean solar time can be interesting to explore,
- from a statistical point of view, we can take look at all the measurements lying further than e.g. three sigma and search for (not only) space weather correlations,
- as the future primary interest are the GRBs, another possibility of examining the data is to look at times when a GRB was not detected by GRBAlpha and understand why,
- to learn more about the secondary rings enhanced by GST, we could look at all the data where it is present, and look for a better threshold for quiet background.

Our analysis has shown that the space weather effects at LEO are large. With more data, the background model will become better. However, the real-time characterization of LEO particle environment will remain challenging as the solar activity is very unpredictable. Nevertheless, there is a lot of yet unexplored points of view, which may reveal new valuable information.

Bibliography

- Angels Aran, Neus Agueda, Alexandr Afanasiev, and Blai Sanahuja. 2018. Charged Particle Transport in the Interplanetary Medium. In *Solar Particle Radiation Storms Forecasting and Analysis (Astrophysics and Space Science Library, Vol. 444)*, Olga E. Malandraki and Norma B. Crosby (Eds.). 63–78. https://doi.org/10.1007/978-3-319-60051-2_4
- D. N. Baker, P. J. Erickson, J. F. Fennell, J. C. Foster, A. N. Jaynes, and P. T. Verronen. 2018. Space Weather Effects in the Earth’s Radiation Belts. 214, 1, Article 17 (Feb. 2018), 17 pages. <https://doi.org/10.1007/s11214-017-0452-7>
- Jason M. H. Beedle, Christopher E. Rura, David G. Simpson, Hale I. Cohen, Valmir P. Moraes Filho, and Vadim M. Uritsky. 2022. A User’s Guide to the Magnetically Connected Space Weather System: A Brief Review. *Frontiers in Astronomy and Space Sciences* 8, Article 253 (Jan. 2022), 253 pages. <https://doi.org/10.3389/fspas.2021.786308>
- Ciarán Beggan, Jim Wild, and Mark Gibbs. 2018. The ground effects of severe space weather. *Astronomy and Geophysics* 59, 4 (Aug. 2018), 4.36–4.39. <https://doi.org/10.1093/astrogeo/aty194>
- Bradley W. Carroll and Dale A. Ostlie. 2006. *An introduction to modern astrophysics and cosmology*.
- P. A. Davidson. 2016. *Kinematics: Advection, Diffusion and Intensification of Magnetic Fields* (2 ed.). Cambridge University Press, 123–143. <https://doi.org/10.1017/9781316672853.009>
- Imke de Pater and Jack J. Lissauer. 2015. *Planetary Sciences*.
- ESA. 2016. Illustration showing Van Allen radiation belts. https://www.esa.int/ESA_Multimedia/Images/2016/06/Illustration_showing_Van_Allen_radiation_belts. Accessed: 2022-05-12.
- ESA/CESAR. 2022. The differential rotation of the Sun and its chromosphere. <https://www.cosmos.esa.int/web/cesar/differential-rotation-and-chromosphere>. Accessed: 2022-05-03.

- R. M. Evans, A. A. Pulkkinen, Y. Zheng, M. Leila Mays, A. Taktakishvili, M. M. Kuznetsova, and M. Hesse. 2013. The SCORE Scale: A Coronal Mass Ejection Typification System Based On Speed. *Space Weather* (June 2013), 333–334. <https://doi.org/10.1002/swe.20058>
- Natalia Ganushkina, Allison Jaynes, and Michael Liemohn. 2017. Space Weather Effects Produced by the Ring Current Particles. 212, 3-4 (Nov. 2017), 1315–1344. <https://doi.org/10.1007/s11214-017-0412-2>
- Nat Gopalswamy. 2017. Extreme Solar Eruptions and their Space Weather Consequences. *arXiv e-prints*, Article arXiv:1709.03165 (Sept. 2017), arXiv:1709.03165 pages. arXiv:1709.03165 [astro-ph.SR]
- John M. Hughes. 2014. *Fundamentals of Space Physics*. http://pages.erau.edu/~reynodb2/ep410/Hughes_FundamentalsOfSpacePhysics.pdf
- A. J. Hundhausen. 1972. Coronal Expansion and Solar Wind. Physics and Chemistry in Space, Vol. 5. Springer, Berlin, Heidelberg.
- J. R. Jokipii and B. Thomas. 1981. Effects of drift on the transport of cosmic rays. IV - Modulation by a wavy interplanetary current sheet. 243 (Feb. 1981), 1115–1122. <https://doi.org/10.1086/158675>
- Sari Katz, Uriel Goldvais, and Colin Price. 2021. The connection between space weather and Single Event Upsets in polar low earth orbit satellites. *Advances in Space Research* 67, 10 (May 2021), 3237–3249. <https://doi.org/10.1016/j.asr.2021.02.007>
- R. S. Kim, K. S. Cho, K. H. Kim, Y. D. Park, Y. J. Moon, Y. Yi, J. Lee, H. Wang, H. Song, and M. Dryer. 2008. CME Earthward Direction as an Important Geoeffectiveness Indicator. 677, 2 (April 2008), 1378–1384. <https://doi.org/10.1086/528928>
- Margaret G. Kivelson and Christopher T. Russell. 1995. *Introduction to Space Physics*.
- Glenn F. Knoll. 2000. *Radiation detection and measurement*.
- Hannu E. J. Koskinen and Emilia K. J. Kilpua. 2022. *Physics of Earth's Radiation Belts: Theory and Observations*. <https://doi.org/10.1007/978-3-030-82167-8>
- NASA. 2002. Advanced Composition Explorer. <https://izw1.caltech.edu/ACE/ASC/DATA/ACEbrochure/ACEbrochure-2nd-ed8.pdf>. Accessed: 2022-05-23.
- NASA. 2015. Reconnection on the Sun. <https://www.nasa.gov/content/goddard/reconnection-on-the-sun>. Accessed: 2022-05-08.
- NASA, NOAA, USAF. 2016. Deep Space Climate Observatory, Earth Science Instrument Overview. https://asdc.larc.nasa.gov/documents/dscovr/DSCOVR_overview_2016-06-29.pdf. Accessed: 2022-05-23.
- NASA/GSFC, NOAA. 2005. NOAA GOES-N,O,P — The Next Generation. https://www.nasa.gov/pdf/112855main_GOESNOPWeb1.pdf. Accessed: 2022-05-04.

- NOAA/SWPC. 2011. The K-index. <https://www.swpc.noaa.gov/sites/default/files/images/u2/TheK-index.pdf>. Accessed: 2022-05-12.
- András. Pál, Masanori Ohno, László Mészáros, Norbert Werner, Jakub Ripa, Marcel Frajt, Naoyoshi Hirade, Ján. Hudec, Jakub Kapuš, Martin Koleda, Robert Laszlo, Pavol Lipovský, Hiroto Mataka, Miroslav Ā melko, Nagomi Uchida, Balázs Csák, Teruaki Enoto, Zsolt Frei, Yasushi Fukazawa, Gábor Galgóczi, Kengo Hirose, Syohei Hisadomi, Yuto Ichinohe, László L. Kiss, Tsunefumi Mizuno, Kazuhiro Nakazawa, Hirokazu Odaka, Hitomitsu Takahashi, and Kento Torigoe. 2020. GRBA α : a 1U CubeSat mission for validating timing-based gamma-ray burst localization. In *Society of Photo-Optical Instrumentation Engineers (SPIE) Conference Series (Society of Photo-Optical Instrumentation Engineers (SPIE) Conference Series, Vol. 11444)*. Article 114444V, 114444V pages. <https://doi.org/10.1117/12.2561351> arXiv:2012.01298 [astro-ph.IM]
- Tuija Pulkkinen. 2007. Space Weather: Terrestrial Perspective. *Living Reviews in Solar Physics* 4, 1, Article 1 (May 2007). <https://doi.org/10.12942/lrsp-2007-1>
- Karel Schrijver, Fran Bagenal, Tim Bastian, Juerg Beer, Mario Bisi, Tom Bogdan, Steve Bougher, David Boteler, Dave Brain, Guy Brasseur, Don Brownlee, Paul Charbonneau, Ofer Cohen, Uli Christensen, Tom Crowley, Debrah Fischer, Terry Forbes, Tim Fuller-Rowell, Marina Galand, Joe Giacalone, George Gloeckler, Jack Gosling, Janet Green, Steve Guetersloh, Viggo Hansteen, Lee Hartmann, Mihaly Horanyi, Hugh Hudson, Norbert Jakowski, Randy Jokipii, Margaret Kivelson, Dietmar Krauss-Varban, Norbert Krupp, Judith Lean, Jeff Linsky, Dana Longcope, Daniel Marsh, Mark Miesch, Mark Moldwin, Luke Moore, Sten Odenwald, Merav Opher, Rachel Osten, Matthias Rempel, Hauke Schmidt, George Siscoe, Dave Siskind, Chuck Smith, Stan Solomon, Tom Stallard, Sabine Stanley, Jan Sojka, Kent Tobiska, Frank Toffoletto, Alan Tribble, Vytenis Vasyliunas, Richard Walterscheid, Ji Wang, Brian Wood, Tom Woods, and Neal Zapp. 2019. Principles Of Heliophysics: a textbook on the universal processes behind planetary habitability. *arXiv e-prints*, Article arXiv:1910.14022 (Oct. 2019), arXiv:1910.14022 pages. arXiv:1910.14022 [astro-ph.SR]
- Manuela Temmer. 2021. Space weather: the solar perspective. *Living Reviews in Solar Physics* 18, 1, Article 4 (Dec. 2021), 4 pages. <https://doi.org/10.1007/s41116-021-00030-3> arXiv:2104.04261 [astro-ph.SR]
- Anna Tenerani. 2012. *DYNAMICS OF ION-SCALE COHERENT MAGNETIC STRUCTURES AND COUPLING WITH WHISTLER WAVES DURING SUBSTORMS*. Ph.D. Dissertation.

